The Astrophysical Journal, 817:144 (30pp), 2016 February 1 doi:10.3847/0004-637X/817/2/144

THE OFFSET AND HOST LIGHT DISTRIBUTIONS OF LONG GAMMA-RAY BURSTS: A NEW VIEW FROM *HST* OBSERVATIONS OF SWIFT BURSTS

Peter K. Blanchard[1], Edo Berger[1], and Wen-fai Fong[2,3]
[1] Harvard-Smithsonian Center for Astrophysics, 60 Garden Street, Cambridge, MA 02138, USA; pblanchard@cfa.harvard.edu
[2] Steward Observatory, University of Arizona, 933 North Cherry Avenue, Tucson, AZ 85721, USA
Received 2015 September 25; accepted 2015 December 9; published 2016 January 28

ABSTRACT

We present the results of an extensive *Hubble Space Telescope* imaging study of 105, mostly *Swift*, long-duration gamma-ray bursts (LGRBs) spanning $0.03 \lesssim z \lesssim 9.4$, which were localized using relative astrometry from ground- and space-based afterglow observations. We measure the distribution of LGRB offsets from their host centers and their relation to the underlying host light distribution. We find that the host-normalized offsets of LGRBs are more centrally concentrated than expected for an exponential disk profile, $\langle R/R_h \rangle = 0.63$, and in particular they are more concentrated than the underlying surface brightness profiles of their host galaxies and more concentrated than supernovae. The fractional flux distribution, with a median of 0.78, indicates that LGRBs prefer some of the brightest locations in their host galaxies but are not as strongly correlated as previous studies indicated. Importantly, we find a clear correlation between offset and fractional flux, where bursts at offsets $R/R_h \lesssim 0.5$ exclusively occur at fractional fluxes $\gtrsim$0.6, while bursts at $R/R_h \gtrsim 0.5$ have a uniform fractional flux distribution. This indicates that the spatial correlation of LGRBs with bright star-forming regions seen in the full sample is dominated by the contribution from bursts at small offset and that LGRBs in the outer parts of galaxies show no preference for unusually bright regions. We conclude that LGRBs strongly prefer the bright, inner regions of their hosts, indicating that the star formation taking place there is more favorable for LGRB progenitor production. This indicates that environmental factors beyond metallicity, such as binary interactions or IMF differences, may operate in the central regions of LGRB hosts.

Key words: gamma-ray burst: general

1. INTRODUCTION

Long-duration gamma-ray bursts (LGRBs) are the most energetic explosions known in the universe, with a volumetric rate of $\lesssim$1% of the core-collapse supernova rate. A wide range of studies of their accompanying afterglow emission and host galaxies has been used to shed light on the properties of the bursts and their progenitors. In particular, the association with broad-lined Type Ic supernovae (Type Ic-BL SNe) and exclusive locations in star-forming galaxies firmly established that LGRBs result from the deaths of massive stars (e.g., Christensen et al. 2004; Woosley & Bloom 2006; Wainwright et al. 2007). Detailed observations of the host galaxies have also indicated a preference for low metallicity environments (Stanek et al. 2006; Levesque et al. 2010a; Graham & Fruchter 2013; Krühler et al. 2015; Perley et al. 2015b), although some bursts occur in environments with solar metallicity (Levesque et al. 2010b, 2010a; Levesque 2012). Similarly, afterglow observations established that LGRBs are powered by relativistic jets with an energy scale of $\sim 10^{51}$ erg (e.g., Frail et al. 2001). These observations support the idea that the progenitors of LGRBs are rapidly rotating massive stars that undergo core collapse to form a hyper-accreting black hole (collapsars; Woosley 1993; MacFadyen & Woosley 1999). However, it is unclear at the present whether these massive stars are single or whether they are subject to a wide range of possible binary interaction scenarios (Podsiadlowski et al. 2004; van den Heuvel & Yoon 2007).

Since direct observations of LGRB progenitors are unlikely due to their low volumetric rate, insight into the nature of the progenitors has to rely on studies of the environments in which LGRBs occur. On a large scale, LGRB hosts have been found to generally be blue, compact, low luminosity, low mass, and low metallicity galaxies with high specific star-formation rates (e.g., Le Floc'h et al. 2003; Christensen et al. 2004; Wainwright et al. 2007; Savaglio et al. 2009; Cucchiara et al. 2015), especially when compared to core-collapse SN hosts (Svensson et al. 2010). These results have led to the notion of a preference for low metallicity progenitors.

The sub-galactic environments of LGRBs can provide additional clues about the nature of the progenitors. To date, two major approaches have been employed in the literature: (i) measuring the offset of LGRBs relative to the centers of their hosts, and (ii) measuring the fractional brightness at the LGRB positions relative to the overall distribution of light within their hosts. In this context, Bloom et al. (2002) combined ground-based afterglow observations and *Hubble Space Telescope* (*HST*) host observations to measure the offsets of 20 LGRBs, and found that they were consistent with being drawn from an exponential disk profile. This led them to conclude that LGRBs were associated with star formation, and to rule out the compact object merger progenitor scenario. However, the small sample size and the large uncertainties in many of the measured offsets prevented a more detailed analysis. Fruchter et al. (2006), on the other hand, argued that the irregular morphologies of at least some LGRB hosts necessitate the use of the fractional brightness technique (hereafter, fractional flux). Using this analysis for 30 LGRB hosts with *HST* observations, in comparison to 16 core-collapse SNe from the GOODS survey, these authors found that LGRBs are more highly concentrated in the brightest regions of their hosts. Svensson et al. (2010) expanded the sample and reached a similar conclusion, including that LGRBs occur in regions with a

[3] Einstein Fellow.

higher surface luminosity compared to core-collapse SNe. These results differ from the conclusion of Bloom et al. (2002) that LGRBs track an exponential light distribution.

In addition to the tension between the results of previous studies, and the relatively small samples used in these studies, it is important to note other potential challenges. First, the aforementioned studies were based on LGRB samples collected from multiple satellites using different trigger criteria, which potentially introduces selection effects that are difficult to quantify. Second, the redshifts were mainly obtained from direct host galaxy spectroscopy (emission lines), leading to a bias toward lower redshifts and more luminous hosts; in conjunction with the small samples, this also limited the ability to probe any redshift evolution in the LGRB locations. Finally, these studies did not include "dark" bursts (i.e., bursts that suffer from large rest-frame extinction), leading to a potential bias against dusty environments; at least on the global scale the hosts of dark bursts appear to be more luminous and massive than the general LGRB host sample (Krühler et al. 2011; Perley et al. 2013). These shortcomings can now be overcome with the much larger and uniform sample of *Swift* LGRBs.

Beyond the direct study of LGRB progenitors, the fractional flux distribution of LGRBs has also been used as a point of comparison with core-collapse SNe. Fruchter et al. (2006) found that the core-collapse SNe from GOODS were consistent with a uniform distribution. Svensson et al. (2010) reached a similar conclusion using a larger sample of GOODS and PANS core-collapse SNe. For more local SN samples, Kelly et al. (2008) measured the fractional flux distributions for Type II and Ib/c SNe, and found that Type Ic SNe are consistent with being drawn from the same fractional flux distribution as LGRBs, whereas Type II and Ib SNe uniformly track the light of their hosts. They suggest that LGRBs and Type Ic SNe share a common progenitor, and that a factor such as metallicity may determine whether core-collapse results in a LGRB with an associated Ic-BL SNe or a normal Type Ic SNe with no associated LGRB. However, recent work has found that LGRBs and Ic-BL SNe occur in host galaxies with high star-formation rate density and that this preference cannot be due to metallicity (Kelly et al. 2014). Finally, the LGRB fractional flux distribution has also been compared to that for super-luminous supernovae, yielding a result that is suggestive of agreement (Lunnan et al. 2015). With the growing samples of SNe, comparative studies of SN and LGRB environments have become limited by the small sample of LGRBs from the studies carried out a decade ago (Bloom et al. 2002; Fruchter et al. 2006). This situation can now be remedied with the much larger sample of *Swift* LGRBs.

Here we present the first uniform analysis of *HST* follow-up observations of the host galaxies of 105 LGRBs collected over the last decade. The goal of this analysis is twofold. First, to investigate the offset and fractional flux distributions for a much larger and more uniform sample of LGRBs than previously possible. Second, to provide a much larger comparison sample for future studies of the locations of other astrophysical transients, such as various SN types. The structure of our paper is as follows. In Section 2 we present the details of the host galaxy and afterglow observations, data analysis, and astrometric matching. In Section 3 we discuss our offset, fractional flux, and host assignment methodologies, and present our measurements. In Section 4 we present our resulting offset and fractional flux distributions, and in Section 5 we discuss potential trends with redshift, the relationship between fractional flux and offset, and implications for LGRB progenitors. We conclude with a summary in Section 6.

In this paper we use $H_0 = 67\,\mathrm{km\,s^{-1}\,Mpc^{-1}}$, $\Omega_m = 0.32$, and $\Omega_\Lambda = 0.68$ (Planck Collaboration et al. 2014), as well as AB magnitudes (Oke & Gunn 1983), corrected for Galactic extinction (Schlafly & Finkbeiner 2011).

2. OBSERVATIONS AND ASTROMETRY

2.1. HST Observations and Reduction

We utilize high resolution *HST* images to locate the LGRBs within their host galaxies. We primarily use Wide Field Camera 3 (WFC3) and Advanced Camera for Surveys (ACS) data, but also Wide Field Planetary Camera 2 (WFPC2) and Near Infrared Camera and Multi Object Spectrometer (NICMOS) data when the former are not available. Our sample is composed of 105 LGRBs, about 91% of which are *Swift* bursts, observed over the last decade (2004 August–2014 October) under multiple programs (see Table 1 for program ID numbers). We perform the first uniform analysis of these data and utilize them for the purpose of investigating the locations of LGRBs within their hosts and their relation to the underlying host light distribution. This sample has the significant advantage of being largely composed of bursts discovered by the *Swift* satellite and thus does not suffer from any potential biases that may be associated with combining data from multiple satellites, as was done in previous studies. About 86% of the bursts in the sample have measured redshifts ($0.03 \lesssim z \lesssim 9.4$) and the *HST* imaging for these bursts span rest-frame UV and optical wavelengths (Figure 1). The wide redshift range allows us to investigate trends as a function of cosmic time. Unlike previous studies, the sample also includes a substantial number of dark LGRBs, which either lack optical afterglows or are much fainter than expected (GRBs 051022, 060719, 060923A, 061222A, 070306, 070521, 070802, 080207, 080325, 080607, 081109, 081221, 090404, 090407, 090417B, 090709A, 100413A, 100615A, 110709B, and 111215A). Some are detected in the NIR, while others are exclusively detected in the radio and X-ray bands.

We retrieved the *HST* observations from the MAST archive; for the ACS images we obtained charge transfer efficiency (CTE) corrected images, while for WFC3/UVIS data we used software from STScI to apply CTE corrections. We reduced the data using the `astrodrizzle` (Gonzaga et al. 2012) task in the STSDAS IRAF package, utilizing recommended parameter settings for each instrument. By combining dithered exposures this task enables the reconstruction of a higher resolution image than that sampled by the instrumental point-spread function. The task also applies distortion corrections to the images, which are critical for precise astrometric alignment. We use `final_pixfrac` = 0.8 and `final_scale` = 0.″065, 0.″02, 0.″03, 0.″05, and 0.″15 per pixel for WFC3/IR, WFC3/UVIS, ACS, WFPC2, and NICMOS, respectively. In Table 1, for each LGRB, we list the program ID, instrument, filter, and exposure time of the final drizzled image. In cases where there are multiple epochs of imaging, we list only the final epoch unless an earlier epoch was chosen as the best host image. In Figure 2 we show the final drizzled image for each burst, with the location of the afterglow shown as determined by relative or absolute astrometry (Sections 2.3 and 2.4).

Table 1
HST and Afterglow Observations

GRB	z	*HST* Image					Afterglow Image	
		Instrument	Filter	Exp. Time (s)	Obs. Date (UT)	Program ID	Telescope	Filter
040701	0.215	ACS/WFC1	F775W	1940	2004 Aug 09	10135	*Chandra*	…
			F625W	1820				
040812	…	ACS/WFC1	F775W	2120	2004 Oct 04	10135	*Chandra*	…
			F625W	2000				
040916	…	ACS/WFC1	F775W	2056	2004 Nov 30	10135	…	…
			F625W	1928				
040924	0.859	ACS/WFC1	F775W	3932	2005 Feb 18	10135	*HST*/ACS/WFC1	F775W
			F850LP	3932	2005 Feb 19			
041006	0.716	ACS/WFC1	F775W	4224	2005 Feb 10	10135	*HST*/ACS/WFC1	F775W
			F850LP	4224	2005 Feb 11			
050315	1.949	WFC3/IR	F160W	1209	2011 Jul 20	12307	*Magellan*/LDSS3	r
050401	2.9	WFC3/IR	F160W	1612	2010 Oct 1	12307	VLT/FORS2	R
050406	2.44	WFC3/IR	F160W	1612	2011 Feb 23	12307	*Magellan*/LDSS3	r
050408	1.236	WFC3/IR	F110W	1012	2013 Mar 24	12949	Gemini-N/GMOS	i
			F160W	1209				
050416A	0.654	ACS/WFC1	F775W	4224	2005 Nov 21	10135	*HST*/ACS/WFC1	F775W
			F850LP					
050525	0.606	ACS/WFC1	F625W	4268	2006 Mar 10	10135	*HST*/ACS/WFC1	F625W
			F775W					
050730	3.967	ACS/WFC1	F775W	7844	2010 Jun 10	11734	LCO/Swope	WashT1
050803	…	WFC3/IR	F160W	906	2011 Sep 3	12307	*Swift*/XRT	…
050820	2.612	ACS/WFC1	F850LP	14280	2006 Jun 8 + 11	10551	*HST*/ACS/WFC1	F850LP
			F625W	2238	2006 Jun 5			
			F775W	4404				
050824	0.83	WFC3/IR	F160W	906	2011 Jan 18	12307	VLT/FORS2	R
050904	6.29	WFC3/IR	F140W	13489	2014 Oct 31	13831	VLT/FORS2	z
050908	3.344	ACS/WFC1	F775W	7892	2010 Oct 31	11734	Gemini-S/GMOS	r
051016B	0.936	WFC3/IR	F160W	906	2011 Jan 16	12307	*Swift*/UVOT	U + B + V
051022	0.8	ACS/WFC1	F606W	1560	2009 Aug 21	11343	*Chandra*	…
		WFC3/IR	F160W	2397	2009 Oct 12			
060115	3.53	ACS/WFC1	F814W	7910	2010 Aug 27	11734	VLT/FORS1	I
060116	…	NICMOS	F160W	5120	2006 Dec 12	10633	*HST*/NICMOS	F160W
			F110W	5120	2006 Dec 11			
		ACS/WFC1	F775W	4400	2006 Oct 10			
			F850LP	1650	2006 Oct 11			
060124	2.296	WFC3/IR	F160W	1612	2010 Sep 28	12307	WHT	I
060206	4.048	ACS/WFC1	F814W	9886	2006 Nov 25	10817	Palomar 60inch	I
060218	0.033	WFC3/IR	F160W	906	2010 Oct 12	12307	*HST*/ACS/WFC1	F625W
		ACS/WFC1	F625W	2040	2006 Oct 26	10551		
			F814W	2040				
			F435W	1530	2006 Nov 04			
			F555W	1020				
060223	4.41	WFC3/IR	F110W	8395	2010 Sep 13	11734	*Swift*/UVOT	V
060418[a]	1.49	ACS/WFC1	F625W	4220	2006 May 09	10551	Self-*HST*	…
			F775W	4220				
			F555W	4386	2006 Jul 13			
060502A	1.51	WFC3/IR	F160W	1209	2010 Oct 11	12307	Gemini-N/GMOS	r
060505[b]	0.089	ACS/WFC1	F475W	27774	2006 May+Jun	10551	Gemini-S/GMOS	g
			F814W	6840	2006 Jun 6 + 7			
		WFC3/IR	F160W	906	2011 Aug 3	12307		
060512[c]	0.443	WFC3/IR	F160W	453	2011 Feb 23	12307	VLT/FORS1	…
060522	5.11	WFC3/IR	F110W	8395	2010 Oct 17	11734	*Swift*/UVOT	White
060526	3.21	ACS/WFC1	F775W	7844	2009 Aug 9	11734	VLT/FORS1	R
060602A	0.787	WFC3/IR	F160W	906	2010 Dec 5	12307	*Swift*/XRT	…
060605	3.78	ACS/WFC1	F775W	7862	2010 Oct 6	11734	TNG	R
060607	3.082	ACS/WFC1	F775W	7910	2010 Sep 17	11734	Gemini-N/GMOS	r
060614	0.125	ACS/WFC1	F606W	3600	2006 Sep 8	10917	*HST*/WFPC2	F606W
			F435W	2152				
			F814W	4840	2006 Oct 31			
		WFC3/IR	F160W	906	2010 Oct 8	12307		
060719	1.532	WFC3/IR	F160W	1209	2013 Feb 24	12949	VLT/FORS2	R
			F125W	1059				
060729	0.54	WFC3/IR	F160W	906	2010 Sep 15	12307	Gemini-S/GMOS	i
060912A	0.937	WFC3/IR	F160W	906	2011 Sep 23	12307	*Swift*/UVOT	White
060923A	…	WFC3/IR	F160W	1198	2013 Feb 10	12949	Gemini-N/NIRI	K

Table 1
(Continued)

GRB	z	*HST* Image					Afterglow Image	
		Instrument	Filter	Exp. Time (s)	Obs. Date (UT)	Program ID	Telescope	Filter
			F125W	1348				
060927	5.6	WFC3/IR	F110W	13992	2010 Sep 25	11734	VLT/FORS2	I
		NICMOS	F160W	10240	2007 Jun 29	10926		
061007	1.261	WFC3/IR	F160W	1209	2011 Jul 8	12307	VLT/FORS1	R
061110A	0.758	WFC3/IR	F160W	906	2010 Sep 30	12307	VLT/FORS1	R
061110B	3.44	ACS/WFC1	F775W	7862	2010 Sep 23	11734	VLT/FORS1	R
061222A	2.088	NICMOS	F160W	7680	2007 Jun 16	10908	Gemini-N/NIRI	K_s
070125	1.547	WFC3/IR	F110W	2812	2010 Apr 24	11717	Gemini-N/GMOS	r
		WFC3/UVIS	F336W	2520				
070208	1.165	WFC3/IR	F160W	1209	2013 Jan 02	12949	Gemini-N/GMOS	r
			F110W	1012				
070306	1.496	WFC3/IR	F160W	1198	2012 Nov 15	12949	VLT/ISAAC	K_s
			F125W	1348				
070318	0.836	WFC3/IR	F160W	906	2010 Dec 31	12307	VLT/FORS1	R
070508	…	WFC3/IR	F160W	906	2011 Feb 22	12307	*Magellan*/MAGIC	I
070521	1.35	WFC3/IR	F160W	906	2011 Aug 02	12307	*Swift*/XRT	…
070721B	3.626	ACS/WFC1	F775W	7844	2010 Nov 13	11734	VLT/FORS2	R
070802	2.45	WFC3/IR	F160W	1209	2013 Feb 22	12949	VLT/FORS2	I
			F105W	1059				
071010A	0.98	WFC3/IR	F160W	906	2010 Oct 29	12307	Keck/LRIS	R
071010B	0.947	WFC3/IR	F160W	906	2010 Nov 25	12307	Gemini-N/GMOS	r
071031	2.692	WFC3/IR	F160W	1612	2010 Nov 20	12307	VLT/FORS2	V
071112C	0.823	WFC3/IR	F160W	906	2010 Oct 08	12307	Gemini-N/GMOS	r
071122	1.14	WFC3/IR	F160W	1209	2010 Dec 21	12307	Gemini-N/GMOS	i
080207	2.086	WFC3/IR	F110W	2397	2009 Dec 09	11343	*Chandra*	…
		WFPC2	F606W	1600	2008 Mar 18			
			F814W	3320	2009 Mar 20			
			F702W	3600	2009 Mar 21			
		NICMOS	F160W	2560	2008 Apr 05			
080319B[d]	0.937	WFPC2	F606W	3200	2008 Jul 03	11513	*HST*/WFPC2	…
			F814W		2008 Jul 05			
080319C	1.95	WFC3/IR	F160W	1209	2010 Sep 19	12307	Gemini-N/GMOS	r
080325	1.78	WFC3/IR	F160W	1209	2012 Dec 31	12949	Subaru/MOIRCS	K_s
			F125W	1359				
080430	0.767	WFC3/IR	F160W	906	2011 Jun 21	12307	*Swift*/UVOT	U+White
080520	1.545	WFC3/IR	F160W	1209	2011 Feb 08	12307	GROND	J
080603A	1.688	WFC3/IR	F125W	1397	2013 Apr 10	12949	Gemini-N/GMOS	r
			F160W	1348				
080603B	2.69	WFC3/IR	F160W	1612	2011 Aug 06	12307	*Swift*/UVOT	U + B + V+W1
080605[b]	1.640	WFC3/IR	F160W	2418	2012 + 2013	12307 + 12949	VLT/FORS2	R
			F125W	1209	2013 Mar 15	12949		
080607	3.036	WFC3/IR	F160W	10791	2010 Jul 25	12005	Palomar 60inch	i
080707	1.23	WFC3/IR	F160W	1209	2010 Oct 31	12307	VLT/FORS1	R
080710	0.845	WFC3/IR	F160W	906	2011 Feb 12	12307	Gemini-S/GMOS	r
080805	1.505	WFC3/IR	F160W	1209	2011 Oct 01	12307	VLT/FORS2	I
080913	6.7	WFC3/IR	F160W	7818	2009 Nov 30	11189	VLT/FORS2	z
080916A	0.689	WFC3/IR	F160W	906	2011 Mar 19	12307	VLT/FORS1	R
080928	1.692	WFC3/IR	F160W	1209	2010 Sep 18	12307	Gemini-S/GMOS	r
081007	0.530	WFC3/IR	F160W	906	2010 Nov 30	12307	Gemini-S/GMOS	r
081008	1.969	WFC3/IR	F160W	1209	2011 Sep 04	12307	Gemini-S/GMOS	r
081109	0.979	WFC3/IR	F110W	1312	2013 Mar 09	12949	GROND	H
			F160W	1359				
081121	2.512	WFC3/IR	F160W	1612	2011 Jan 04	12307	GROND	r
081221	2.26	WFC3/IR	F160W	1209	2013 Jun 17	12949	Gemini-N/NIRI	K
			F105W	1209				
090113	1.749	ACS/WFC1	F606W	2208	2009 Oct 15	11840	WHT/LIRIS	K
		WFC3/IR	F160W	2612	2009 Oct 17			
090404	...	WFC3/IR	F160W	2612	2010 Jan 09	11840	PdBI	108 GHz
			F105W	1359	2013 Jul 06	12949		
			F125W	1209				
		ACS/WFC1	F606W	2208	2010 Sep 02	11840		
090407	1.449	WFC3/IR	F160W	1209	2010 Sep 15	11840	*Chandra*	…
		WFC3/UVIS	F606W	740				
090417B	0.345	WFC3/IR	F160W	2612	2009 Oct 17	11840	*Swift*/XRT	…
		ACS/WFC1	F606W	1656	2011 Jan 22			

Table 1
(Continued)

GRB	z	*HST* Image					Afterglow Image	
		Instrument	Filter	Exp. Time (s)	Obs. Date (UT)	Program ID	Telescope	Filter
090418A	1.608	WFC3/IR	F160W	1209	2010 Oct 02	12307	*Swift*/UVOT	U
090423[b]	8.2	WFC3/IR	F160W	42997	2010 + 2011	11189	Gemini-N/NIRI	H
			F125W	52117	2010			
090424	0.544	WFC3/IR	F160W	906	2011 May 03	12307	Gemini-S/GMOS	r
090429B[b]	9.4	WFC3/IR	F160W	4823	2010 Jan+Feb	11189	Gemini-N/NIRI	...
			F105W	4823	2010 Feb 24 + 28			
		ACS/WFC1	F606W	2100	2010 Jan 03			
090618	0.54	WFC3/IR	F160W	906	2011 Jan 09	12307	Palomar 60inch	I
090709A	…	WFC3/IR	F160W	1359	2012 Oct 15	12949	Subaru/MOIRCS	K_s
			F125W	1397				
091127	0.49	WFC3/IR	F160W	906	2010 Dec 16	12307	Gemini-S/GMOS	i
091208B	1.063	WFC3/IR	F160W	1209	2010 Oct 10	12307	Gemini-N/GMOS	r
100205A	…	WFC3/IR	F160W	1209	2010 Dec 06	11840	Gemini-N/NIRI	K
		WFC3/UVIS	F606W	1140				
100316D	0.059	WFC3/UVIS	F336W	1680	2011 Aug 03	12323	*HST*/WFC3/UVIS	F336W
			F225W	2520	2011 Aug 02			
			F438W	1230				
			F814W	1260				
			F275W	2520	2011 Aug 03			
			F555W	1680				
			F625W	720	2011 Aug 06			
			F763M	1720				
		WFC3/IR	F125W	1312	2011 Aug 02			
			F160W	1312				
		ACS/WFC1	FR716N	2400	2011 Aug 06			
100413A	…	WFC3/IR	F160W	1209	2010 Aug 31	11840	EVLA	8.5 GHz
		WFC3/UVIS	F606W	752				
100526A	…	WFC3/IR	F125W	1348	2013 Jun 30	12949	Gemini-N/NIRI	K
			F160W	1209				
100615A	1.398	WFC3/UVIS	F606W	1128	2010 Dec 16	11840	*Chandra*	…
		WFC3/IR	F160W	1209				
100621A	0.542	WFC3/IR	F160W	909	2013 Mar 09	12949	VLT/XSHOOTER	I
			F105W	748				
			F125W	898				
100905A	…	WFC3/IR	F140W	5440	2013 Jul 10	12247	…	…
110312A	…	WFC3/IR	F160W	1209	2011 Nov 18	12378	*Swift*/XRT	…
		WFC3/UVIS	F606W	1110	2011 Nov 17			
110709B	…	WFC3/UVIS	F606W	2480	2011 Nov 08	12378	*Chandra*	…
		WFC3/IR	F160W	2612	2011 Nov 12			
110731A	2.83	WFC3/UVIS	F625W	5200	2012 Aug 22	12370	*HST*/WFC3/UVIS	F625W
111215A	2.06	WFC3/UVIS	F606W	1110	2013 May 13	12764	*Chandra*	…
		WFC3/IR	F160W	1209				
120119A	1.728	WFC3/IR	F160W	1209	2012 Oct 08	12949	Gemini-S/GMOS	r
			F125W	1209				
120711A	1.405	WFC3/UVIS	F625W	8400	2013 Aug 18	12749	*HST*/WFC3/UVIS	F625W
120923A	…	WFC3/IR	F140W	10423	2013 May 01	12558	*HST*/WFC3/IR	F140W
130427A	0.340	WFC3/UVIS	F606W	2396	2014 May 15	13117	*HST*/WFC3/UVIS	F606W
		WFC3/IR	F160W	3621				
130925A	0.347	WFC3/UVIS	F814W	2400	2014 Aug 18	13611	*HST*/WFC3/UVIS	F814W
		WFC3/IR	F110W	1212				
			F160W					

Notes. The table is organized such that the first image listed for each burst is the image for which the corresponding offset and fractional flux measurements were used to compile the distribution (Section 4). For bursts with multiple observations, we group the observations by instrument. Within an instrument group, the observations are listed by date. Only the last epoch of observations is shown for bursts with multiple epochs, unless an earlier epoch was chosen as the best host image. Blank entries in the table indicate inheritance of the entry in the previous row.

[a] The afterglow and what we believe to be the host galaxy (Pollack et al. 2009) are both detected in the same epoch and offset from each other, such that centroid measurements are not biased. Therefore the offset (see Section 3.1) can be measured using this single early epoch image. To measure the fractional flux (see Section 3.4) we used a late epoch image where the afterglow has faded away.

[b] We combined multiple epochs in the same filter to obtain deep images. For GRB 060505, the afterglow was not detected in early epoch *HST* observations, so we combined these observations with a later epoch.

[c] The *HST* data for GRB 060512 is of poor quality, preventing further analysis.

[d] We combined the F606W and F814W filters to obtain a higher S/N detection of the host. The afterglow image is also a stack of these two filters at an earlier epoch.

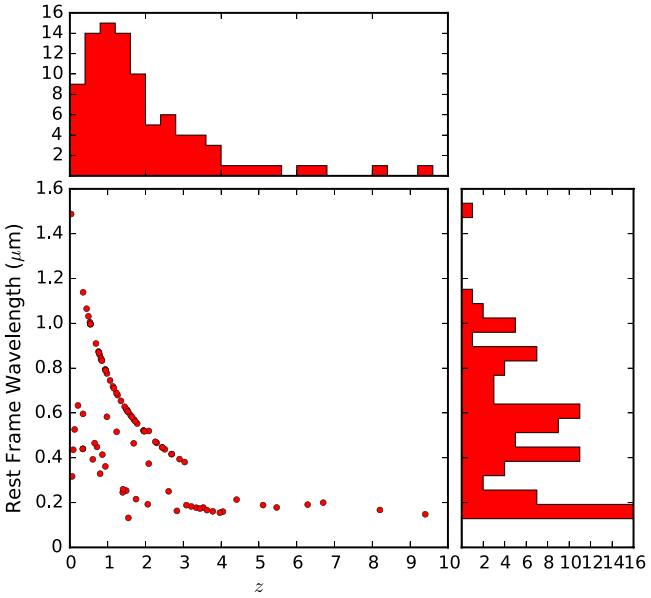

Figure 1. Rest-frame wavelength vs. redshift of the observations used to measure offsets and fractional flux for each LGRB. Only bursts with measured redshifts are included in this plot. Also shown are the projected histograms of the redshift distribution and the distribution of rest-frame wavelengths probed by the *HST* observations.

2.2. Afterglow Imaging

To precisely locate the LGRBs within their host galaxies requires the detection of an afterglow. About 85% of bursts in the sample have detected optical or NIR afterglows. We utilize the deepest, highest resolution afterglow images available to best match the quality of *HST* imaging. We primarily rely on publicly available afterglow images from the 8 m Very Large Telescope (VLT) and 8 m Gemini North and South telescopes. In 16 cases, an afterglow image is available from *HST*. We also use images from the *Swift* UV/Optical Telescope (UVOT), 6.5 m *Magellan* telescopes, Palomar 60 inch Telescope, Swope 40 inch Telescope, 8.2 m Subaru Telescope, 4.2 m William Herschel Telescope (WHT), 3.6 m Telescopio Nazionale Galileo (TNG), 10 m Keck telescopes, and the 2.2 m MPG/ESO Telescope using the Gamma-Ray Burst Optical/Near-Infrared Detector (GROND).

We use standard IRAF packages to analyze the afterglow data. We use the task `uvotimsum` in the HEASoft package to co-add *Swift*/UVOT images, combining multiple filters if necessary to obtain a high signal-to-noise ratio (S/N) afterglow detection. For *HST* afterglow images, we use `astrodrizzle` as described in Section 2.1. For GRB 070306 we use the `eclipse` pipeline to reduce the NIR data from VLT/ISAAC. For GRBs 080325 and 090709A we use the MCSRED IRAF package to reduce the NIR data from Subaru/MOIRCS. For the remaining bursts without optical or NIR afterglows, we rely on radio or X-ray detections. We obtain the reported radio positions from the GCN circular archive. When an X-ray afterglow image is available from *Chandra*, we retrieve the image from the *Chandra* Data Archive. For each burst, we list in Table 1 the telescope and filter utilized to obtain the afterglow image that was used for astrometry.

2.3. Relative Astrometry

We use relative astrometry to precisely locate the afterglows on the *HST* images. We first identify common point-like sources between the afterglow and *HST* images, using `SExtractor` (Bertin & Arnouts 1996) to measure the source positions. We then match the coordinates with the IRAF task `ccmap`, using a second or third order polynomial to compute the astrometric solution. Using the afterglow images from the telescopes listed in Section 2.2, we generally obtain the following astrometric tie uncertainties, $\sigma_{\rm tie}$ (1σ):

1. 6 mas using an *HST* detection of an optical or NIR afterglow.
2. 30 mas using an optical or NIR afterglow detection from ground-based telescopes.
3. 100 mas using a UV or optical afterglow detection from *Swift*/UVOT.
4. 300 mas using an X-ray afterglow detection from *Chandra*.

In a few cases, the lack of sufficient common sources for a robust astrometric tie necessitates the use of an intermediate image to locate the afterglow position on the *HST* image. This is the case for bursts detected with *Chandra*. We use the CIAO task `wavdetect` to measure the positions of X-ray sources. In these cases, the uncertainty associated with the match between the *Chandra* and intermediate ground-based images dominates the total astrometric tie uncertainty. Table 2 lists the number of common sources and astrometric tie uncertainty for each burst. Bursts with no listed astrometric tie uncertainty are those for which the best afterglow position is from XRT or for which we were not able to obtain an afterglow image. GRB 060418 is a unique case where the afterglow and host are well-detected in a single *HST* image and are sufficiently offset from one another such that the position of one is not biased by the light distribution of the other. Therefore astrometric matching is not necessary for this burst.

2.4. Absolute Astrometry

In cases where the afterglow is detected only in the radio band, or when the X-ray observations do not contain any common sources for relative astrometry, absolute astrometry is performed by matching the late-time *HST* images to the 2MASS astrometric system. This is mainly the case for dark GRBs. For the two GRBs where a radio position was used (090404 and 100413A), the uncertainty in the afterglow position with respect to the *HST* image is dominated by the astrometric accuracy of those radio positions, $\sim 0\farcs5$. Similarly, when using absolute astrometry to locate the X-ray afterglow of GRB 090407, the error is dominated by the astrometric accuracy of *Chandra*, $\sim 0\farcs4$.

3. MEASUREMENT METHODOLOGY

3.1. Offset Measurements

Once the afterglow and *HST* images are registered, we identify the host galaxy in the *HST* image. First we measure the afterglow centroid using `SExtractor` to determine the afterglow position relative to the *HST* image. The afterglow positional uncertainty ($\sigma_{\rm AG}$) is estimated as $\frac{\rm FWHM}{2({\rm S/N})}$. In some cases, it is apparent in the afterglow image that there is an underlying extended object, presumably the host galaxy. To

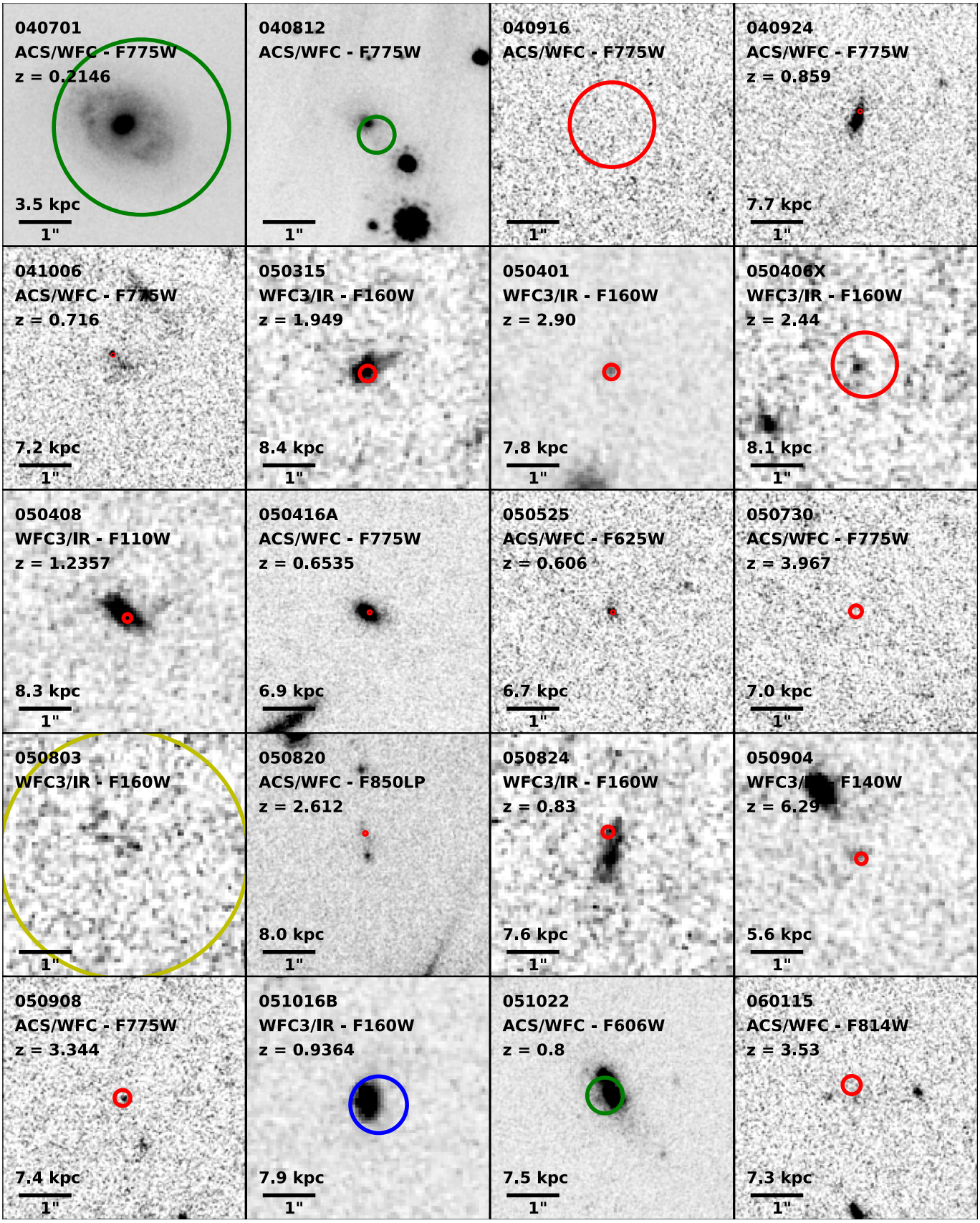

(a) Panel One

Figure 2. *Hubble Space Telescope* drizzled images of 105 LGRB host galaxies studied in this work. The circles (3σ) indicate the location of each GRB. North is up and East is to the left. Red, blue, green, cyan, and yellow circles indicate that afterglow positions were determined from optical/NIR, *Swift*/UVOT, *Chandra*, radio, and XRT images, respectively. Physical scales are given when the LGRB redshift is known.

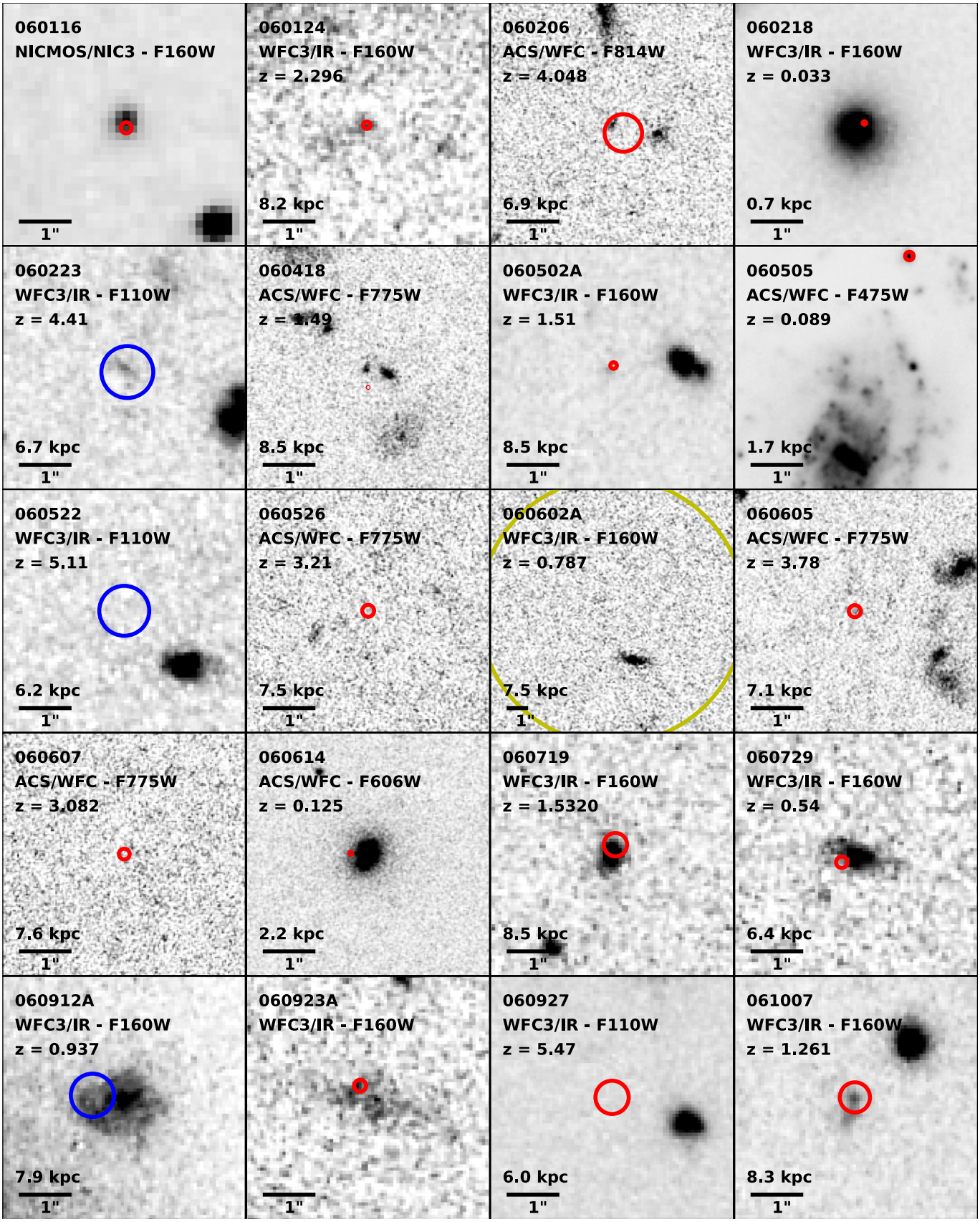

(b) Panel Two

Figure 2. (Continued.)

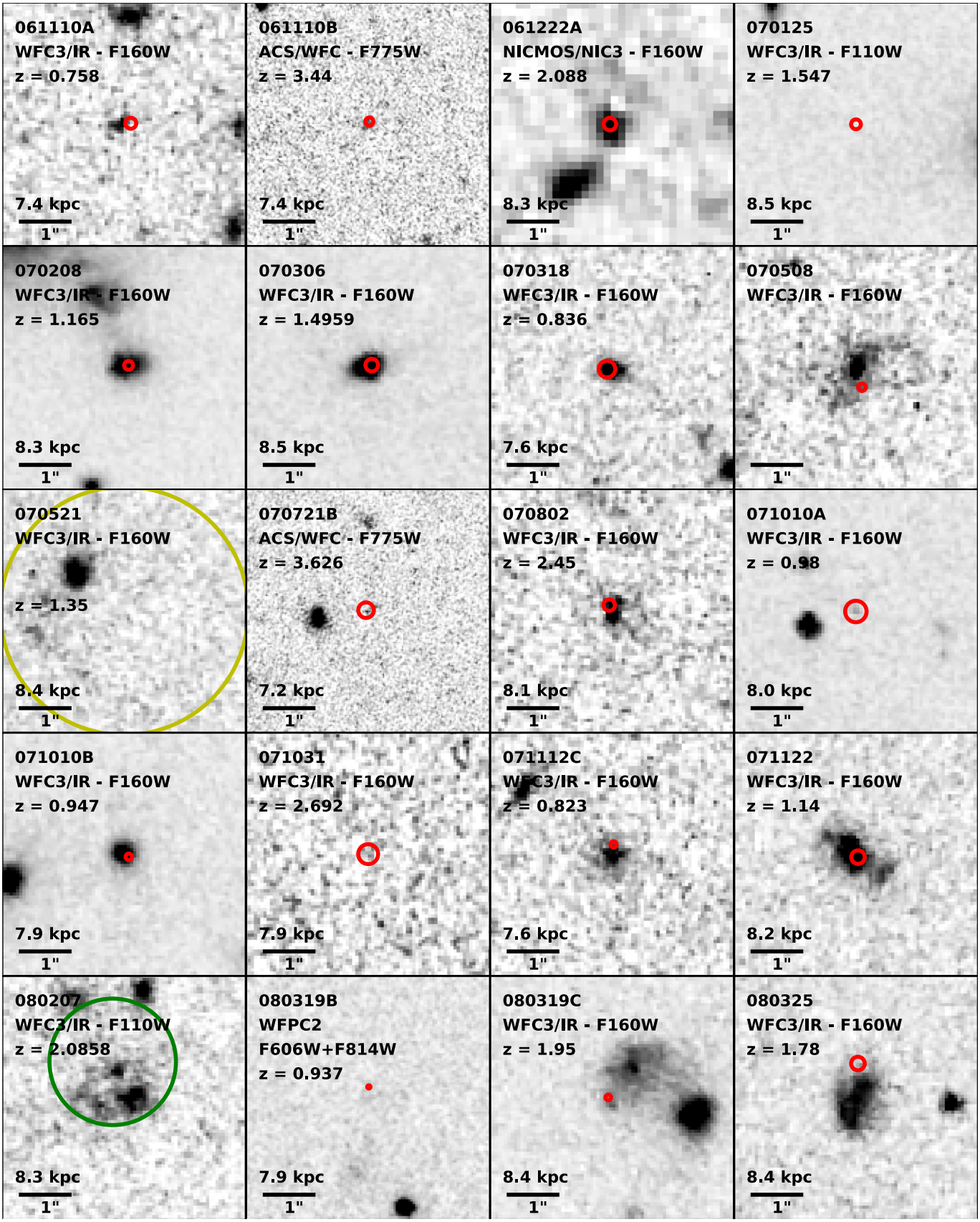

(c) Panel Three

Figure 2. (Continued.)

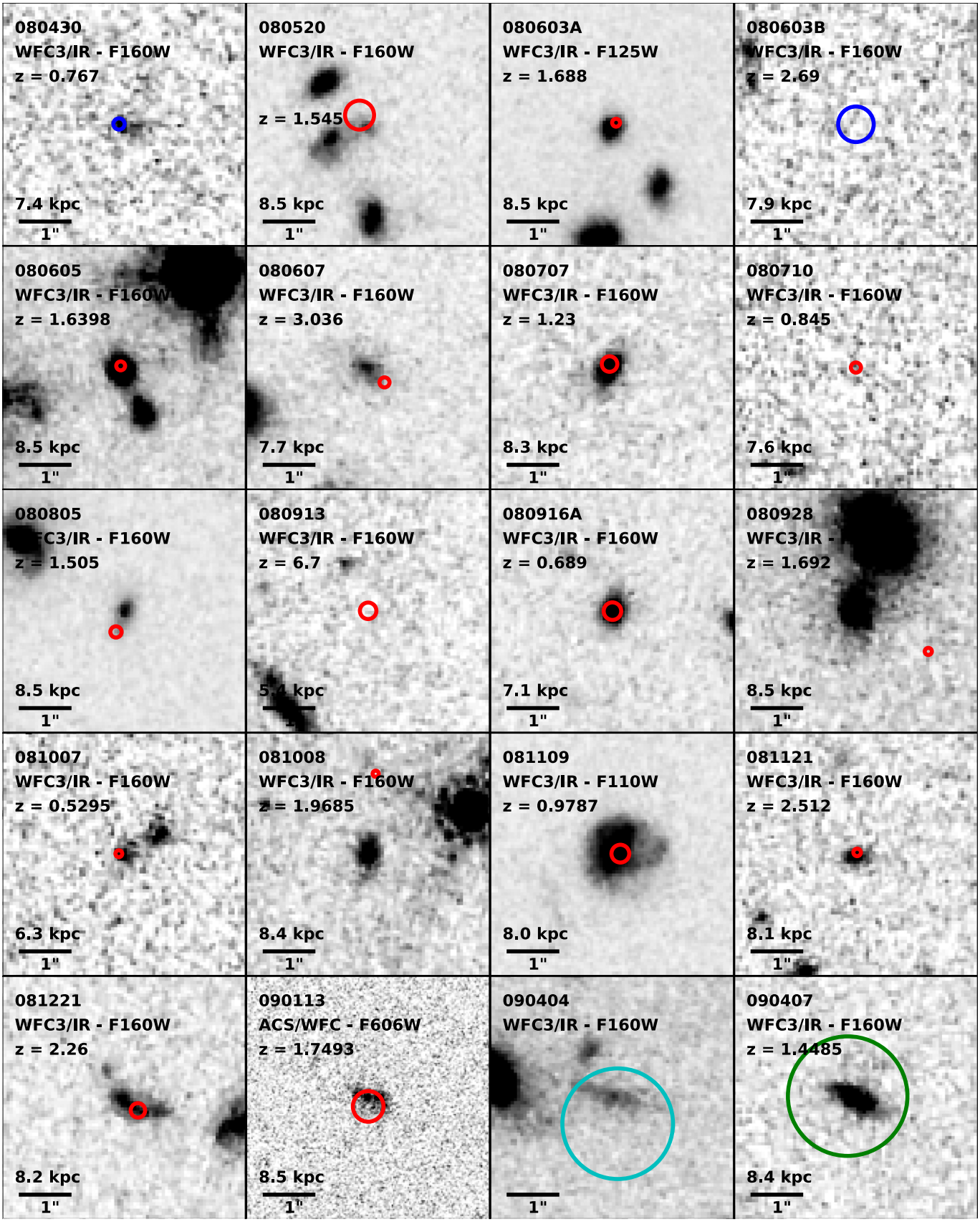

(d) Panel Four

Figure 2. (Continued.)

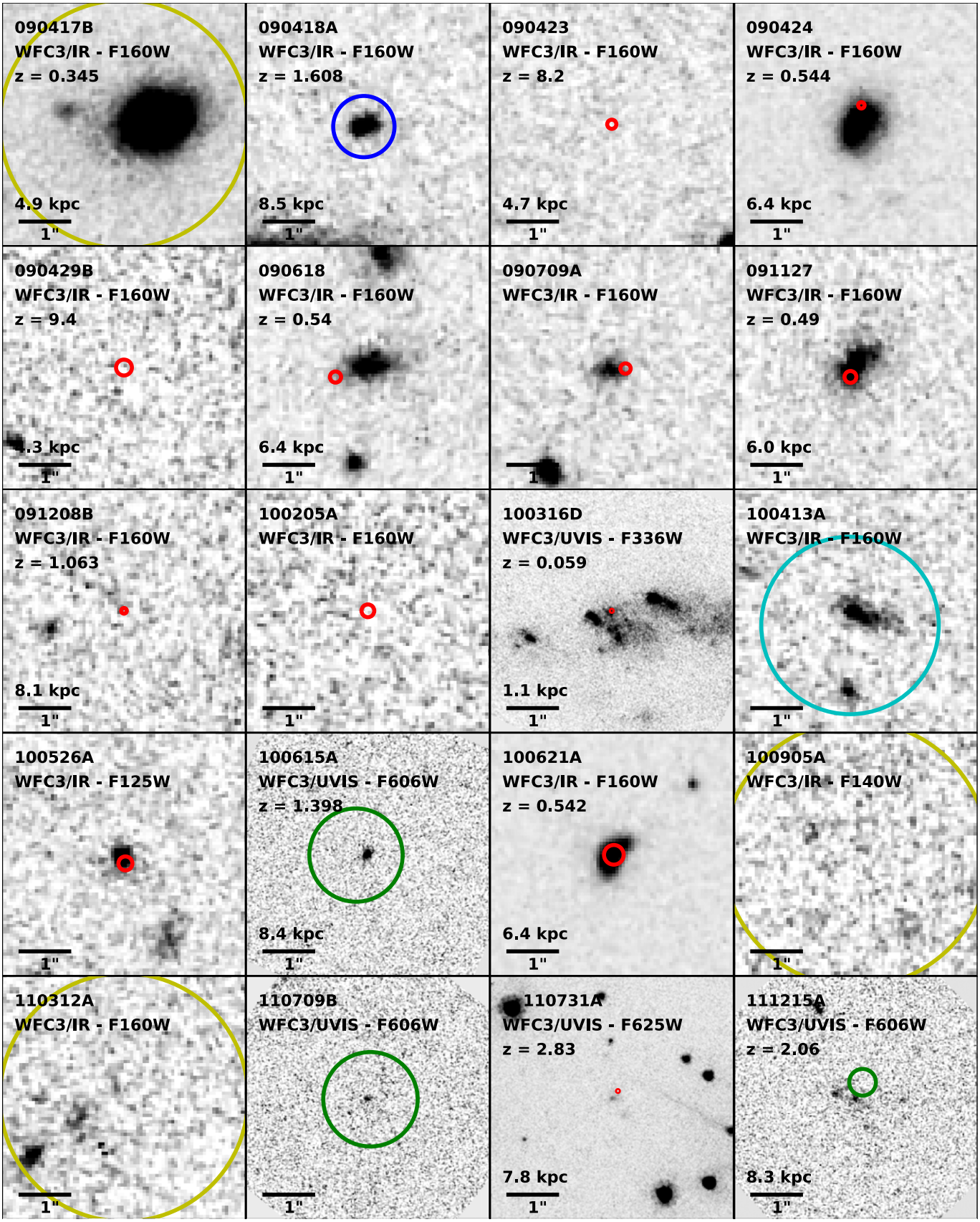

(e) Panel Five

Figure 2. (Continued.)

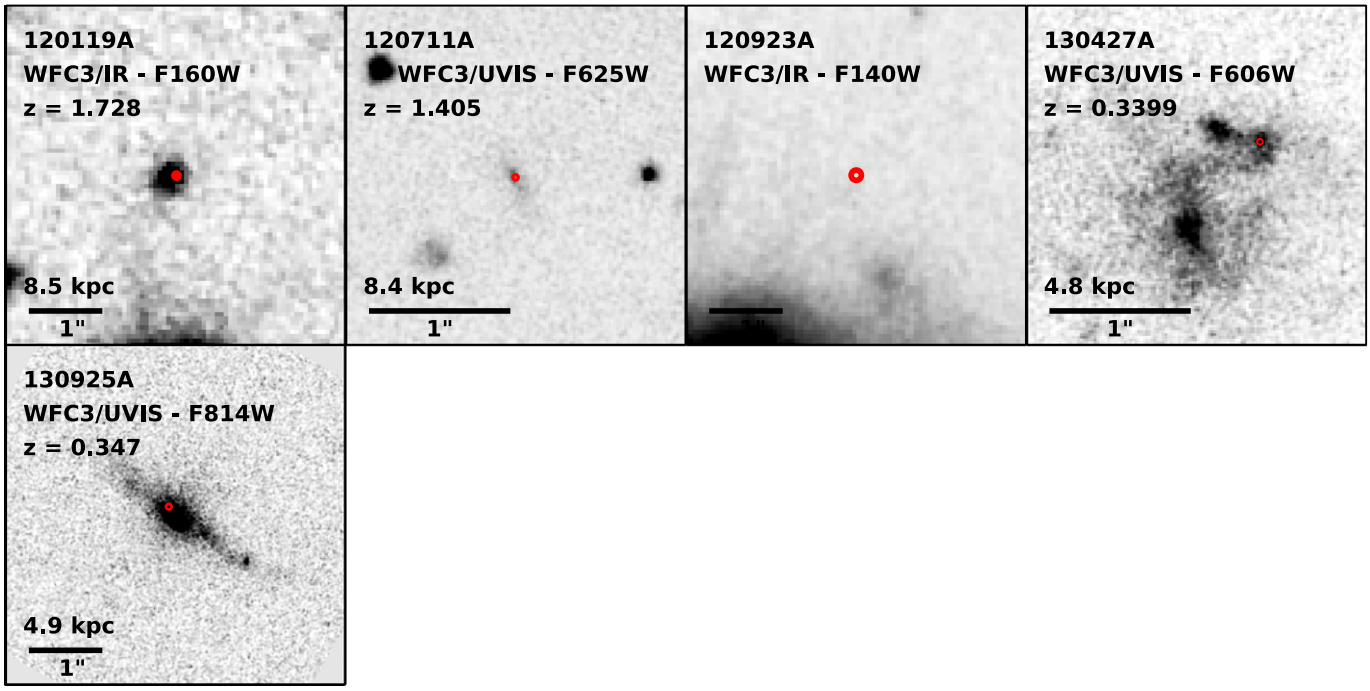

(f) Panel Six

Figure 2. (Continued.)

reliably measure the centroid of the afterglow, we perform image subtraction, using the ISIS software package (Alard 2000), relative to a late-time image of the host, ideally from the same telescope and in the same filter. Once the afterglow position is determined, we use a uniform host assignment procedure discussed in Section 3.3. Here we continue our discussion of the offset measurement procedure, assuming a host galaxy has been identified.

We measure the host galaxy center and corresponding uncertainty using `SExtractor`. We use a uniform definition of the host center as the brightest region of the galaxy (or peak of the light distribution) determined by sequentially increasing the threshold for detection in `SExtractor`. The statistical uncertainty on the centroid determined by `SExtractor` does not take into account the larger systematic uncertainties caused by the fact that LGRB hosts tend to have irregular morphologies. Instead, the uncertainty on the host center ($\sigma_{\rm host}$) is estimated by taking the quadrature sum of the standard deviation in both directions of the positions measured by multiple runs of `SExtractor` using varying thresholds for detection from 3σ to the highest threshold that yields a detection.

Using the afterglow position and host center, we calculate the projected angular offset (R) between the afterglow position and host center. The total uncertainty on the angular offset (σ_R) is taken to be the quadrature sum of $\sigma_{\rm tie}$, $\sigma_{\rm AG}$, and $\sigma_{\rm host}$. We also calculate the projected physical offsets using the measured redshift for each burst. For bursts with no measured redshift, we use the fact that at $z \gtrsim 0.5$, which is typical of most LGRBs, the angular diameter distance is approximately constant so that we can use a conversion factor of about 8 kpc/″. The projected angular and physical offsets and corresponding uncertainties are listed in Table 2. Bursts for which no offsets are listed indicate either bursts with well-localized afterglows but no detected host (see Section 3.3 for a discussion of distinguishing between no host detection and a large offset) or bursts for which we only have an XRT position or were unable to access the afterglow image. The uncertainties on the XRT positions are typically $\gtrsim 1''$ in radius, which is too large to enable a reliable host association.

3.2. Host Galaxy Sizes, Normalized Offsets, and Magnitudes

As our interest lies in the positions of LGRBs relative to the light of their host galaxies, we normalize the offsets by the sizes of the hosts. Here we use the half-light radius (R_h) as measured by `SExtractor` (with `FLUX_RADIUS` = 0.5). We also measure the 80% light radius (R_{80}) for comparison with previous studies of LGRBs and SNe. In Table 2, we list the half-light radii and host-normalized offsets ($R_{\rm norm}$) for each burst.

We also measure the apparent magnitudes of the host galaxies and corresponding uncertainties using the MAG_AUTO estimate from `SExtractor`, which uses Kron apertures. We obtain the magnitude zeropoints from STScI where tabulated, or from the photometry keywords in the *HST* image headers. The magnitudes corrected for Galactic extinction (Schlafly & Finkbeiner 2011) and corresponding uncertainties are listed in Table 2 for each burst with an associated host galaxy.

3.3. Host Galaxy Assignment

To assign host galaxies to each LGRB, we calculate the probability of chance coincidence for several candidate extended objects surrounding the afterglow position, given the observed number density of field galaxies from deep optical and NIR surveys (Hogg et al. 1997; Beckwith et al. 2006; Metcalfe et al. 2006). Nominally we assign the candidate with

Table 2
Offsets, Galaxy Sizes, Magnitudes, and P_{cc}

GRB	# Tie Objects	σ_{tie} ($''$)	σ_{AG} ($''$)	σ_{host} ($''$)	R ($''$)	R_{phys} (kpc)	R_h ($''$)	R_{norm}	AB Mag[a]	P_{cc}
040701	4	0.367	0.475	…	…	…	…	…	…	…
040812	5	0.115	0.046	0.019	0.270 ± 0.125	2.283 ± 1.057	0.297	0.908 ± 0.420	19.450 ± 0.010	<0.001
040916	…	…	0.150	…	…	…	…	…	>27.1	…
040924	41	0.005	0.002	0.014	0.286 ± 0.015	2.197 ± 0.116	0.188	1.521 ± 0.080	23.954 ± 0.024	0.003
041006[b]	24	0.004	<0.001	0.007	0.352 ± 0.008	2.536 ± 0.061	0.298	1.180 ± 0.029	24.668 ± 0.057	0.012
050315	17	0.054	0.003	0.017	0.114 ± 0.056	0.953 ± 0.474	0.236	0.481 ± 0.239	23.808 ± 0.029	0.006
050401	24	0.044	0.025	0.009	0.082 ± 0.051	0.638 ± 0.397	0.170	0.483 ± 0.300	25.217 ± 0.077	0.006
050406	7	0.038	0.217	0.006	0.195 ± 0.220	1.579 ± 1.788	0.121	1.609 ± 1.822	26.602 ± 0.140	0.041
050408	14	0.027	0.002	0.010	0.152 ± 0.029	1.263 ± 0.239	0.278	0.545 ± 0.103	23.700 ± 0.022	0.008
050416A	24	0.007	<0.001	0.011	0.037 ± 0.013	0.260 ± 0.090	0.160	0.234 ± 0.081	23.001 ± 0.009	0.001
050525	74	0.006	0.001	0.002	0.028 ± 0.007	0.185 ± 0.046	0.119	0.232 ± 0.057	26.067 ± 0.064	0.004
050730	9	0.038	0.014	…	…	…	…	…	>27.9	…
050803	…	…	0.850	…	…	…	…	…	…	…
050820	28	0.009	0.003	0.004	0.442 ± 0.010	3.530 ± 0.081	0.116	3.808 ± 0.087	25.196 ± 0.050	0.009
050824	6	0.036	0.012	0.038	0.473 ± 0.054	3.597 ± 0.410	0.402	1.177 ± 0.134	23.716 ± 0.042	0.021
050904	8	0.036	0.006	0.004	0.139 ± 0.037	0.774 ± 0.205	0.150	0.928 ± 0.246	27.888 ± 0.101	0.018
050908	15	0.054	0.001	0.003	0.037 ± 0.055	0.275 ± 0.405	0.068	0.544 ± 0.802	27.669 ± 0.136	0.006
051016B	4	0.062	0.184	0.013	0.257 ± 0.194	2.023 ± 1.532	0.228	1.127 ± 0.853	22.314 ± 0.011	0.004
051022	5	0.121	0.015	0.021	0.171 ± 0.124	1.283 ± 0.932	0.334	0.512 ± 0.372	22.020 ± 0.006	0.002
060115	18	0.045	0.043	0.017	0.280 ± 0.065	2.042 ± 0.471	0.125	2.239 ± 0.517	27.342 ± 0.137	0.026
060116	10	0.024	0.029	…	…	…	…	…	>27.1	…
060124	16	0.020	0.016	0.025	0.034 ± 0.035	0.278 ± 0.291	0.172	0.197 ± 0.206	26.133 ± 0.126	0.009
060206	6	0.127	0.021	0.005	0.292 ± 0.128	2.021 ± 0.888	0.091	3.211 ± 1.411	27.647 ± 0.094	0.035
060218	13	0.012	<0.001	0.044	0.174 ± 0.045	0.115 ± 0.030	0.606	0.287 ± 0.075	19.635 ± 0.003	0.002
060223	9	0.173	0.041	0.009	0.112 ± 0.178	0.749 ± 1.186	0.211	0.532 ± 0.844	26.534 ± 0.069	0.026
060418	…	…	0.003	0.004	0.404 ± 0.005	3.419 ± 0.040	0.118	3.425 ± 0.040	25.855 ± 0.067	0.013
060502A	8	0.021	0.009	0.006	0.051 ± 0.023	0.435 ± 0.198	0.162	0.317 ± 0.144	25.864 ± 0.110	0.007
060505	20	0.029	0.004	0.023	4.307 ± 0.037	7.160 ± 0.062	1.195	3.605 ± 0.031	19.101 ± 0.001	0.009
060522	4	0.089	0.146	…	…	…	…	…	>28.9	…
060526	23	0.040	0.006	…	…	…	…	…	>27.4	…
060602A	…	…	2.550	…	…	…	…	…	…	…
060605	29	0.041	0.004	0.002	0.025 ± 0.041	0.180 ± 0.294	0.109	0.232 ± 0.379	27.555 ± 0.148	0.011
060607	33	0.037	0.003	…	…	…	…	…	>28.9	…
060614	21	0.009	0.002	0.011	0.357 ± 0.014	0.801 ± 0.031	0.329	1.086 ± 0.042	22.821 ± 0.007	0.003
060719	12	0.051	0.062	0.011	0.206 ± 0.081	1.743 ± 0.684	0.246	0.837 ± 0.328	23.400 ± 0.023	0.006
060729	17	0.039	0.001	0.015	0.338 ± 0.042	2.149 ± 0.265	0.308	1.098 ± 0.135	23.509 ± 0.028	0.011
060912A	11	0.148	0.005	0.036	0.654 ± 0.153	5.155 ± 1.203	0.713	0.918 ± 0.214	21.547 ± 0.013	0.017
060923A	38	0.039	0.013	0.052	0.291 ± 0.066	2.460 ± 0.560	0.696	0.418 ± 0.095	23.278 ± 0.038	0.039
060927	18	0.026	0.111	…	…	…	…	…	>28.6	…
061007	5	0.026	0.100	<0.001	0.022 ± 0.103	0.184 ± 0.862	0.373	0.059 ± 0.277	23.621 ± 0.033	0.013
061110A	11	0.035	0.014	0.015	0.135 ± 0.040	0.992 ± 0.297	0.176	0.765 ± 0.229	25.114 ± 0.083	0.007
061110B	49	0.025	0.011	0.011	0.061 ± 0.030	0.449 ± 0.220	0.104	0.586 ± 0.288	27.230 ± 0.105	0.008
061222A	15	0.026	0.034	0.011	0.044 ± 0.044	0.368 ± 0.368	0.193	0.229 ± 0.229	24.399 ± 0.050	0.005
070125	5	0.033	0.007	…	…	…	…	…	>28.0	…
070208	6	0.030	0.006	0.025	0.099 ± 0.040	0.820 ± 0.327	0.368	0.270 ± 0.108	21.902 ± 0.009	0.005
070306	14	0.043	0.005	0.011	0.090 ± 0.045	0.760 ± 0.380	0.209	0.430 ± 0.215	21.860 ± 0.007	0.002
070318	8	0.057	0.007	0.019	0.109 ± 0.060	0.827 ± 0.458	0.205	0.529 ± 0.293	24.100 ± 0.034	0.005
070508	16	0.025	0.004	0.020	0.423 ± 0.033	3.577 ± 0.277	0.592	0.714 ± 0.055	22.871 ± 0.031	0.026
070521	…	…	0.850	…	…	…	…	…	…	…
070721B	17	0.042	0.032	0.006	0.045 ± 0.054	0.327 ± 0.387	0.057	0.793 ± 0.939	28.442 ± 0.165	0.011
070802	10	0.039	0.007	0.027	0.132 ± 0.048	1.069 ± 0.390	0.348	0.379 ± 0.138	23.994 ± 0.043	0.014
071010A	9	0.039	0.062	0.009	0.013 ± 0.074	0.106 ± 0.590	0.162	0.082 ± 0.457	25.311 ± 0.111	0.005
071010B	7	0.022	0.001	0.010	0.109 ± 0.025	0.860 ± 0.195	0.257	0.424 ± 0.096	22.635 ± 0.016	0.004
071031	7	0.068	<0.001	…	…	…	…	…	>27.4	…
071112C	10	0.020	0.007	0.017	0.202 ± 0.027	1.533 ± 0.206	0.398	0.508 ± 0.068	23.674 ± 0.046	0.016
071122	10	0.032	0.033	0.025	0.075 ± 0.053	0.616 ± 0.433	0.393	0.191 ± 0.134	22.678 ± 0.017	0.009
080207	2	0.381	0.206	0.066	0.769 ± 0.438	6.402 ± 3.650	0.683	1.126 ± 0.642	23.225 ± 0.025	0.047
080319B	18	0.011	0.001	0.117	0.215 ± 0.118	1.697 ± 0.929	0.147	1.465 ± 0.802	26.679 ± 0.200	0.015
080319C	10	0.018	0.008	0.004	0.078 ± 0.020	0.655 ± 0.167	0.145	0.538 ± 0.137	25.298 ± 0.047	0.005
080325	60	0.022	0.041	0.059	0.697 ± 0.075	5.890 ± 0.635	0.443	1.574 ± 0.170	22.537 ± 0.016	0.017
080430	4	0.035	0.015	0.030	0.108 ± 0.049	0.800 ± 0.361	0.282	0.384 ± 0.173	24.595 ± 0.071	0.012
080520	52	0.050	0.086	0.024	0.258 ± 0.102	2.181 ± 0.865	0.223	1.155 ± 0.458	23.965 ± 0.032	0.007
080603A	22	0.027	<0.001	0.013	0.089 ± 0.030	0.753 ± 0.255	0.202	0.440 ± 0.149	22.884 ± 0.011	0.003

Table 2
(Continued)

GRB	# Tie Objects	$\sigma_{\rm tie}$ ($''$)	$\sigma_{\rm AG}$ ($''$)	$\sigma_{\rm host}$ ($''$)	R ($''$)	$R_{\rm phys}$ (kpc)	R_h ($''$)	$R_{\rm norm}$	AB Mag[a]	$P_{\rm cc}$
080603B	6	0.117	0.034	…	…	…	…	…	>26.7	…
080605	38	0.029	0.009	0.008	0.081 ± 0.031	0.682 ± 0.266	0.198	0.407 ± 0.159	22.467 ± 0.008	0.002
080607	7	0.033	0.011	0.024	0.454 ± 0.042	3.482 ± 0.320	0.419	1.083 ± 0.099	24.372 ± 0.027	0.029
080707	6	0.047	0.024	0.009	0.089 ± 0.054	0.739 ± 0.449	0.263	0.338 ± 0.205	22.950 ± 0.017	0.005
080710	6	0.035	<0.001	…	…	…	…	…	>26.1	…
080805	15	0.038	0.006	0.026	0.466 ± 0.047	3.944 ± 0.396	0.275	1.695 ± 0.170	23.249 ± 0.020	0.010
080913	13	0.035	0.044	…	…	…	…	…	>28.0	…
080916A	12	0.056	0.022	0.010	0.011 ± 0.061	0.075 ± 0.432	0.240	0.044 ± 0.254	22.762 ± 0.016	0.004
080928	16	0.021	0.012	0.016	1.705 ± 0.029	14.437 ± 0.245	0.442	3.858 ± 0.066	21.990 ± 0.010	0.035
081007	11	0.023	<0.001	0.017	0.111 ± 0.029	0.700 ± 0.182	0.277	0.402 ± 0.105	24.489 ± 0.059	0.011
081008	28	0.021	0.002	0.018	1.658 ± 0.028	13.902 ± 0.236	0.236	7.027 ± 0.119	23.591 ± 0.028	0.065
081109	8	0.052	0.032	0.002	0.171 ± 0.061	1.364 ± 0.486	0.545	0.314 ± 0.112	21.519 ± 0.006	0.008
081121	15	0.026	0.002	0.011	0.042 ± 0.028	0.342 ± 0.226	0.198	0.214 ± 0.142	24.923 ± 0.054	0.007
081221	11	0.047	0.016	0.055	0.388 ± 0.074	3.195 ± 0.609	0.409	0.949 ± 0.181	23.156 ± 0.025	0.015
090113	8	0.073	0.075	0.001	0.186 ± 0.105	1.573 ± 0.888	0.294	0.633 ± 0.357	24.304 ± 0.028	0.007
090404	4	0.115	0.361	0.044	0.556 ± 0.381	4.709 ± 3.229	0.690	0.806 ± 0.553	23.370 ± 0.018	0.045
090407	5	0.134	0.387	0.021	0.172 ± 0.410	1.451 ± 3.463	0.336	0.511 ± 1.220	22.953 ± 0.019	0.026
090417B	…	…	0.850	…	…	…	…	…	…	…
090418A	5	0.209	0.014	0.017	0.096 ± 0.211	0.812 ± 1.785	0.214	0.448 ± 0.984	23.687 ± 0.025	0.009
090423	6	0.031	0.005	…	…	…	…	…	>28.2	…
090424	9	0.021	0.005	0.030	0.407 ± 0.037	2.594 ± 0.235	0.407	1.000 ± 0.090	21.260 ± 0.007	0.005
090429B	10	0.053	0.012	…	…	…	…	…	>28.1	…
090618	12	0.038	0.001	0.025	0.693 ± 0.046	4.402 ± 0.292	0.519	1.335 ± 0.089	22.464 ± 0.020	0.020
090709A	25	0.028	0.021	0.007	0.283 ± 0.036	2.393 ± 0.305	0.256	1.105 ± 0.141	24.213 ± 0.038	0.010
091127	16	0.040	0.005	0.028	0.221 ± 0.049	1.335 ± 0.296	0.411	0.538 ± 0.119	22.700 ± 0.021	0.011
091208B	7	0.019	0.001	…	…	…	…	…	>26.7	…
100205A	12	0.034	0.028	…	…	…	…	…	>26.7	…
100316D[c]	15	0.007	<0.001	<0.001	…	…	…	…	…	…
100413A	8	0.098	0.600	…	…	…	…	…	…	…
100526A	10	0.047	0.008	0.008	0.194 ± 0.049	1.645 ± 0.411	0.188	1.034 ± 0.258	24.766 ± 0.033	0.007
100615A	3	0.318	0.028	0.004	0.246 ± 0.320	2.073 ± 2.694	0.083	2.963 ± 3.850	25.092 ± 0.033	0.031
100621A	6	0.062	0.025	0.015	0.045 ± 0.069	0.284 ± 0.439	0.262	0.17 ± 0.263	21.316 ± 0.006	0.002
100905A	…	…	0.910	…	…	…	…	…	…	…
110312A	…	…	0.850	…	…	…	…	…	…	…
110709B	1	0.318	0.057	0.005	0.067 ± 0.323	0.564 ± 2.737	0.073	0.912 ± 4.430	26.714 ± 0.080	0.105
110731A	211	0.006	0.001	0.008	0.182 ± 0.010	1.423 ± 0.082	0.121	1.502 ± 0.087	25.236 ± 0.043	0.004
111215A	2	0.075	0.052	0.002	0.341 ± 0.091	2.844 ± 0.763	0.210	1.624 ± 0.435	25.086 ± 0.044	0.010
120119A	49	0.013	<0.001	0.012	0.012 ± 0.017	0.099 ± 0.146	0.202	0.058 ± 0.086	23.480 ± 0.022	0.004
120711A	78	0.004	0.001	0.015	0.016 ± 0.016	0.137 ± 0.133	0.153	0.106 ± 0.103	25.606 ± 0.034	0.005
120923A	59	0.008	0.024	…	…	…	…	…	>27.8	…
130427A	6	0.001	<0.001	0.007	0.828 ± 0.007	4.013 ± 0.033	0.634	1.306 ± 0.011	21.866 ± 0.007	0.007
130925A	8	0.006	0.002	0.008	0.156 ± 0.010	0.765 ± 0.051	0.355	0.439 ± 0.029	21.783 ± 0.008	0.001

Notes. For bursts with multiple *HST* images of the host galaxy, the image used to make the measurements listed here corresponds to the first image listed for the burst in Table 1. We show the 3σ upper limits for bursts with no host detection. Bursts with no listed offset or upper limit correspond to those bursts for which we were not able to obtain a suitable afterglow image.

[a] Magnitudes are corrected for Galactic extinction (Schlafly & Finkbeiner 2011).

[b] The SN associated with GRB 041006 is detected in the final epoch. The SN and host center are sufficiently offset from each other, such that centroid measurements are not biased. However, measurement of fractional flux is not possible.

[c] GRB 100316D occurred in a low redshift galaxy with irregular morphology. The complexity of the host system prevents a meaningful definition of the host center. We therefore do not make an offset measurement for this burst.

the lowest probability of chance coincidence as the host. Candidates at small offsets from the afterglow position, such that the afterglow position is essentially coincident with the candidate, will in most cases have the lowest probability of chance coincidence. Bursts for which there are no coincident candidates require further investigation to distinguish between the scenario where the host was not detected and the scenario where the burst occurred at a large offset from a neighboring galaxy. We discuss these cases in detail in Section 3.3.1.

Following the methodology of Bloom et al. (2002), we determine the probability of chance coincidence ($P_{\rm cc}$) using the following equation:

$$P_{\rm cc} = 1 - e^{-\pi R_e^2 \sigma(\leqslant m)} \quad (1)$$

where $\sigma(\leqslant m)$ is the observed number density of galaxies brighter than magnitude m and R_e is the effective radius. For optical observations we use the galaxy number densities given by Equation (1) of Berger (2010), whereas for NIR

observations we use the H-band number counts measured by Metcalfe et al. (2006). As discussed by Bloom et al. (2002), the appropriate value of R_e depends on the offset, size of the galaxy, and uncertainty on the afterglow position. Following Bloom et al. (2002) we take R_e to be the maximum of $(3\sqrt{\sigma_{\rm tie}^2+\sigma_{\rm OT}^2}, \sqrt{R^2+4R_h^2})$. In other words, if the localization is precise, such that the first term is much smaller than the offset and galaxy size, then the second term dominates. On the other hand, if the GRB localization is poor, the positional uncertainty dominates over the offset and galaxy size and its radius becomes the appropriate value of the effective radius for determining $P_{\rm cc}$. In the majority of cases ($\sim$87%) the localizations are sufficiently precise such that the second term dominates over the first. As discussed in Section 2.3, $\sigma_{\rm tie}$ is typically $\gtrsim$100 mas for bursts when we use afterglow detections from *Swift*/UVOT or *Chandra*. In these cases, the GRB positional uncertainty can dominate over the offset and galaxy size.

We list the values of $P_{\rm cc}$ in Table 2. For the bursts with coincident extended objects, $P_{\rm cc}$ tends to fall in the range 10^{-3} to 5×10^{-2}. Therefore we do not expect significant contamination of our host galaxy sample by unrelated galaxies along the line of sight.

3.3.1. Bursts With No Coincident Host Candidate

The subset of bursts that lack a coincident extended object must be examined further to determine if the object with the lowest $P_{\rm cc}$ can realistically be considered the host galaxy. Relying simply on $P_{\rm cc}$ may result in the inclusion of unrealistically luminous objects in the sample. We identify the nearest extended objects with $P_{\rm cc}\lesssim 0.1$ as possible host candidates. Given the measured redshift of the burst, we can determine whether the luminosity of the host candidate is consistent with the range of LGRB host luminosities observed at that redshift. It may be more likely that the true host lies beyond the magnitude limit of our observations and is not detected. However, it is important to avoid biasing our results by eliminating potential large offsets. Here we discuss our assessment of bursts whose host candidates satisfy $P_{\rm cc}\lesssim 0.1$ but are offset by significantly more than the half-light radius of the host candidate.

To carry out the assessment of non-coincident host candidates with $P_{\rm cc}\lesssim 0.1$, we compare their luminosities to the luminosities of the coincident host galaxies. We convert our measured apparent magnitudes to rest-frame luminosities in units of L^*. Given the redshift, we determine the absolute magnitude and using measured values of L^* from galaxy surveys (Faber et al. 2007; Marchesini et al. 2007; Bouwens et al. 2015) we calculate L/L^* for each host galaxy. For bursts with $z\lesssim 1.7$ we use the measured value of L^* in the B-band for the blue galaxy sample analyzed by Faber et al. (2007). In the range $1.7\lesssim z\lesssim 3.2$ we use L^* values in the B-band from Marchesini et al. (2007) using their $U-V<0.25$ mag galaxy subsample. For bursts with $z\gtrsim 3.2$, we use L^* corresponding to UV bands as measured by surveys of Lyman-break galaxies (Bouwens et al. 2015). These were chosen so that the wavelength regime in which the L^* values are appropriate corresponds roughly to the rest-frame wavelengths probed by our observations in these redshift bins. We do not perform a K-correction to a common band.

We plot the luminosities as a function of redshift for the full sample, including coincident and non-coincident candidates, in the left panel of Figure 3. The right panel shows the luminosities as a function of host-normalized offset. The luminosities of the robust host galaxy associations span $\sim(0.01-1)L^*$, whereas some host candidates at relatively large offset and high $P_{\rm cc}$ have luminosities ranging from $\sim(3-100)L^*$, which is inconsistent with the distribution for bursts with coincident host galaxies, indicating that they are unrelated galaxies. The luminosity of the host candidate for GRB 060526 is $\sim100L^*$ assuming it is at the redshift of the GRB; this is much larger than expected for a GRB host. We therefore reject this association. We also reject the candidates for GRBs 060927, 070125, 071031, and 091208B because their luminosities are unreasonably high given the observed distribution for securely assigned hosts. In the case of GRB 080928, there are two candidates with $P_{\rm cc}\lesssim 0.1$ where the object with $P_{\rm cc}\approx 0.023$ has a luminosity of $\sim4L^*$ and the object with $P_{\rm cc}\approx 0.035$ has a luminosity of $\sim L^*$. We therefore accept the lower luminosity galaxy as the host. We also accept the candidate for GRB 081008 as the host due to its reasonable luminosity of $\sim0.6L^*$. The left panel of Figure 3 also shows upper limits on the luminosities of the hosts where we are confident that the host was not detected due to the lack of any nearby host candidates with $P_{\rm cc}\lesssim 0.1$. Upper limits for the cases with the rejected host candidates discussed above are also shown.

Furthermore, we note that there is no trend of host luminosity versus host-normalized offset. There is no reason to suspect from predictions that bursts at large or small offsets occur only in bright or faint galaxies. As shown in Figure 3, the inclusion of the rejected host candidates creates an artificial trend because the only galaxies at higher normalized offset that have $P_{\rm cc}\lesssim 0.1$ are bright galaxies. Therefore we are confident that these rejected candidates are unrelated galaxies and the true host was not detected. Indeed, the resulting upper limits on the luminosities of these hosts are not surprising, given the upper limits we calculate for unambiguous non-detected hosts. Upon completing our host assignment procedure, we obtain a sample size of 79 LGRBs for which we make offset and fractional flux measurements.

3.4. Fractional Flux Measurements

Studying the locations of LGRBs within their hosts can be expanded beyond an analysis of the offset distribution. In many cases where the host's morphology is irregular, the location of the host center is unclear and the offset from an empirically defined center may not be meaningful. Furthermore, the host galaxy size defined by the half-light radius does not capture the complex morphology of many of the hosts. While measuring offsets is useful for comparing the locations of LGRBs with the predicted profiles of star formation, we would like to go one step further and ask whether or not LGRBs are spatially coincident with sites of massive star formation. This is possible using a method, which is less sensitive to galaxy morphology than offsets, of comparing the brightness at the LGRB location relative to the entire host light distribution (Fruchter et al. 2006). We calculate the fraction of the total flux from the host galaxy that is contained in pixels fainter than or equal to the flux at the LGRB location. The resulting "fractional flux" is a statistic that measures the brightness of the burst site compared to the entire galaxy. A fractional flux value of one

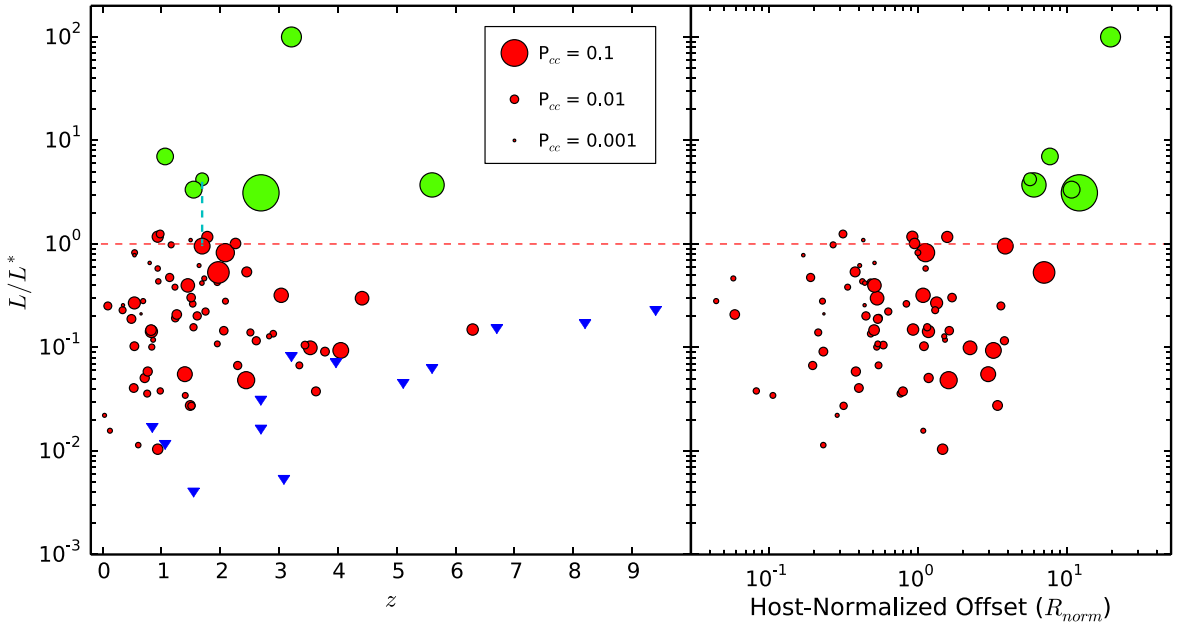

Figure 3. Left: host galaxy rest-frame luminosity in units of L^* as a function of redshift for assigned host galaxies (red), rejected host candidates (green), and non-detected hosts (blue). The data point area is proportional to P_{cc}, where a smaller point means a smaller P_{cc}. The red dotted line indicates a luminosity of L^*, and the dotted cyan line connects the two possible host candidates for GRB 080928 (see Section 3.3.1). We do not include bursts with unknown redshift. Right: host galaxy luminosity vs. host-normalized offset. As expected, this is a scatter plot for the robust host associations. The correlated tail caused by the rejected candidates is an indication that they are unrelated galaxies.

means that the burst occurred on the brightest pixel in the galaxy.

We measure the fractional flux for each LGRB using the following procedure: First, we determine the flux value at the LGRB position. When the 1σ error circle defined by the uncertainty on the LGRB position as determined by the quadrature sum of $\sigma_{\rm tie}$ and $\sigma_{\rm AG}$ spans less than a pixel, we simply take the flux value of that pixel. When the error circle encompasses more than one pixel but is smaller than the point-spread function (PSF), we measure an average flux within the 1σ error circle weighted by the fractional area encompassed by a given pixel. These scenarios are relevant for most bursts where we use afterglows from ground-based optical/NIR telescopes and *HST* (see Section 2). We use `SExtractor` to extract the host galaxy pixels using a threshold of 1σ above the sky background and then calculate the fraction of the total flux in pixels fainter than or equal to the average flux of the LGRB error region (the fractional flux).

When the error circle is larger than the PSF, the galaxy brightness as a function of position could vary significantly, so that the uncertainty in the position of the LGRB may have a large impact on the fractional flux. This scenario is often encountered when using optical afterglow detections from *Swift*/UVOT, X-ray afterglows from *Chandra*, or radio afterglow detections, where the error regions can encompass tens to hundreds of pixels. In some cases, these pixels include both the faintest and brightest pixels of the host galaxy. In this regime, it is unclear whether the fractional flux determined as described above remains a meaningful quantity. Here, we show that for bursts with error circles larger than the PSF, a different weighting is required to properly assess the fractional flux in these cases.

To assess this, we employ a different procedure for determining the fractional flux, taking into account the Gaussian error distribution associated with each burst. As before we extract the galaxy pixels using `SExtractor`. Each pixel in the image has an associated probability for hosting the burst, governed by the 2D Gaussian distribution that takes into account the astrometric tie and afterglow positional uncertainties. A corresponding fractional flux value can be calculated for all pixels encompassed by the error circle. Pixels not associated with the galaxy will have fractional flux values of zero. The posterior probability distribution for the fractional flux can then be constructed by weighting each value by its corresponding Gaussian probability. The fractional flux and corresponding uncertainty are estimated as the mean and standard deviation of this distribution.

By comparing the fractional flux values for bursts with large error regions with the well-localized bursts, we find that there exists a considerable bias toward lower fractional flux values in the former. We hypothesize that the absolute size of the error circle is important, as well as the error circle size relative to the galaxy size. If the galaxy is much larger than the error circle, even a large error circle in an absolute sense can yield a well-constrained fractional flux value. If a relatively well-localized burst occurs in a small galaxy, the fractional flux value may not be well-constrained. Figure 4 illustrates this bias by plotting the fractional flux versus the ratio of error circle area to galaxy area (left panel). The right panel of Figure 4 shows the cumulative distributions for two subsets of the data divided at an area ratio of 0.1. Of the bursts with area ratios $\gtrsim$0.1, there are none with fractional flux values $\gtrsim$0.86, whereas $\sim$30% of bursts with an area ratio of $\lesssim$0.1 have fractional flux values $\gtrsim$86. This bias can be understood by noting that as the error region increases relative to the galaxy size, there is a greater probability that the burst occurred on background sky pixels. In general, we find that for error regions that are large in an absolute or relative sense, there is a bias toward lower fractional flux values. To avoid biasing our results, we remove the bursts with area ratios of $\gtrsim$0.1 from consideration, reducing the sample size to 57

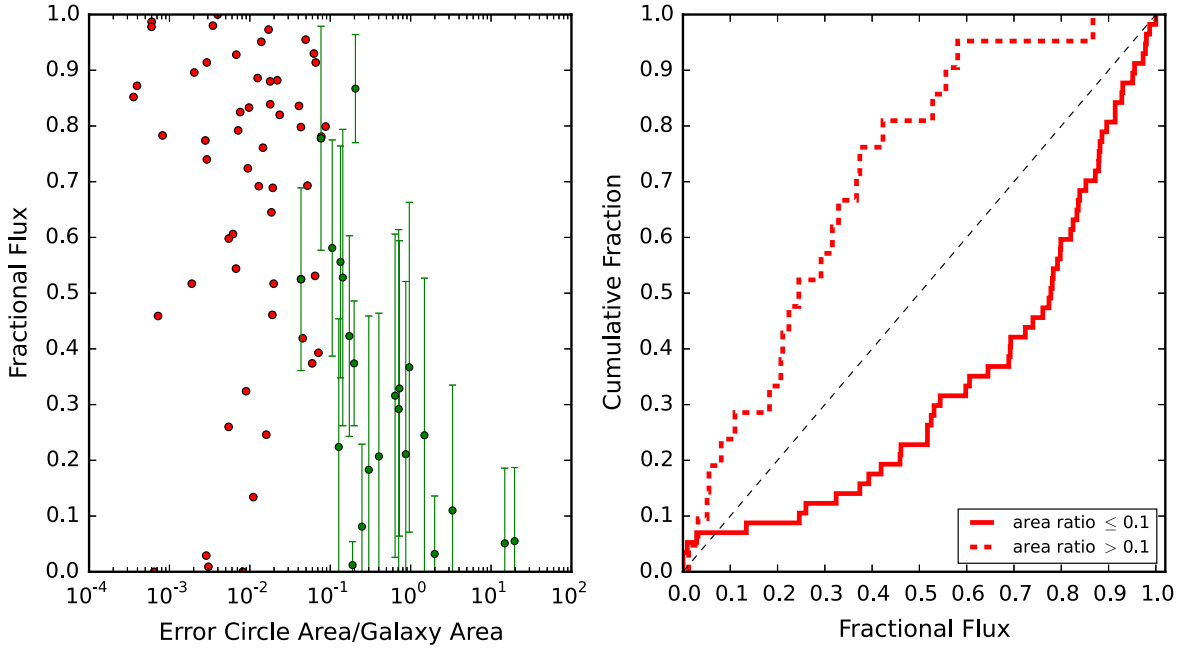

Figure 4. Left: fractional flux vs. the ratio of the error circle area to galaxy area. Green points with error bars represent bursts with error circles larger than the *HST* PSF. Right: the fractional flux distribution binned into two bins separated at an area ratio of 0.1. In both plots it is apparent that there is a bias to lower fractional flux values when the error circle covers a substantial fraction of the galaxy area. In the analysis in Section 4.2 we only use bursts with a ratio of $\lesssim$0.1.

LGRBs. By removing these bursts, we are not concerned about selecting against bursts with intrinsically low fractional flux values. Here we are removing a bias associated with the measurement of fractional flux when burst localization is poor.

In Table 3 we list the fractional flux values and area ratios for each LGRB. Bursts with no fractional flux value are either bursts for which a host was not detected or a sufficient afterglow position was not available.

4. RESULTS

We compiled the largest sample of LGRB offsets and fractional flux measurements presented to date. Our aim is to use them to understand where LGRBs occur within their host galaxies and what the results from a large sample indicate about the progenitors. Here we present the results of our offset and fractional flux distribution measurements summarized in Tables 2 and 3. In the following discussion we present the results of empirical distribution comparisons using the Kolmogorov–Smirnov (KS) test and Anderson–Darling (AD) test. We include the KS test due to its wide use in previous works, but regard the AD test as a more robust statistical measure.

4.1. Offset Distribution

In this section we present the measured physical and host-normalized offset distributions. We also present the results of an analysis of the offset uncertainties to understand how they affect the offset distributions. Each offset measurement has an associated uncertainty (σ_R) dependent on $\sigma_{\rm tie}$, $\sigma_{\rm AG}$, and $\sigma_{\rm host}$ (Section 3.1). Due to the inherent non-Gaussian nature of offsets and the non-uniform uncertainties, we employ a Monte Carlo approach to assess the uncertainty on the resulting distributions of offsets. At each iteration, a random offset (x) was drawn for each burst from its offset probability distribution defined by the measured offset (R) and uncertainty (σ_R). For bursts with $R/\sigma_R \lesssim 5$ we use a Rice distribution to represent the probability distributions, defined by:

$$p(x|R,\,\sigma_R) \;=\; \frac{x}{\sigma_R^2}\exp\left[-\frac{(x^2+R^2)}{2\sigma_R^2}\right]I_0\left(\frac{xR}{\sigma_R^2}\right) \qquad (2)$$

where I_0 is the zeroth order modified Bessel function of the first kind. For $R/\sigma_R \gtrsim 5$, the Rice distribution can be approximated as a Gaussian. We make this approximation for numerical ease. In all cases discussed in the following sections, we use 10,000 iterations.

4.1.1. Physical Offset Distribution

In Figure 5 we show the cumulative distribution of projected physical offsets, calculated as described in Section 3.1. The final sample size included in this distribution is 79 LGRBs, which is the subset of the original sample where offset measurement is possible. The distribution ranges from offsets of 0.075 to 14.4 kpc with the median at 1.28 kpc. About 90% of bursts occur within ~5 kpc. The distribution is remarkably smooth and has bursts representing the full range of offsets. There are few gaps where we do not find bursts, with one notable gap at ~7–14 kpc. For comparison, we also show the distribution of physical offsets for the small sample of 20 LGRBs measured by Bloom et al. (2002). The two distributions agree exceptionally well. KS and AD tests yield p-values of 0.79 and 0.94, respectively. We also show in Figure 5 the results of our Monte Carlo simulation (taking into account the offset uncertainties) by plotting a 2D histogram showing the density of points from the resulting cumulative distributions generated at each iteration. Darker regions indicate a higher density of points; in other words, a high fraction of synthetic distributions pass through that region. The apparent shift of the distribution from the measured distribution toward higher offset values is indicative of the skew to higher offsets resulting from

Table 3
Fractional Flux and Ratio of Error Circle to Galaxy Area

GRB	Fractional Flux	Ratio	GRB	Fractional Flux	Ratio
040701	…	…	071031	…	…
040812	0.423	1.74×10^{-1}	071112C	0.774	2.83×10^{-3}
040916	…	…	071122	0.951	1.37×10^{-2}
040924	0.783	8.21×10^{-4}	080207	0.207	4.02×10^{-1}
041006	…	1.80×10^{-4}	080319B	0.598	5.65×10^{-3}
050315	0.693	5.25×10^{-2}	080319C	0.839	1.85×10^{-2}
050401	0.799	8.86×10^{-2}	080325	0.134	1.10×10^{-2}
050406	0.11	3.31	080430	0.645	1.82×10^{-2}
050408	0.724	9.48×10^{-3}	080520	0.374	1.99×10^{-1}
050416A	0.896	1.91×10^{-3}	080603A	0.880	1.79×10^{-2}
050525	0.914	2.61×10^{-3}	080603B	…	…
050730	…	…	080605	0.820	2.35×10^{-2}
050803	…	…	080607	0.544	6.89×10^{-3}
050820	0.606	6.69×10^{-3}	080707	0.836	4.03×10^{-2}
050824	0.324	8.91×10^{-3}	080710	…	…
050904	0.374	5.92×10^{-2}	080805	0.517	1.96×10^{-2}
050908	0.316	6.31×10^{-1}	080913	…	…
051016B	0.329	7.25×10^{-1}	080916A	0.930	6.28×10^{-2}
051022	0.556	1.33×10^{-1}	080928	0.009	2.99×10^{-3}
060115	0.081	2.48×10^{-1}	081007	0.792	6.89×10^{-3}
060116	…	…	081008	0.000	7.99×10^{-3}
060124	0.882	2.22×10^{-2}	081109	0.886	1.26×10^{-2}
060206	0.032	2.00	081121	0.973	1.73×10^{-2}
060218	0.872	3.92×10^{-4}	081221	0.761	1.47×10^{-2}
060223	0.292	7.10×10^{-1}	090113	0.224	1.27×10^{-1}
060418	0.000	6.46×10^{-4}	090404	0.183	3.02×10^{-1}
060502A	0.689	1.99×10^{-2}	090407	0.245	1.49
060505	0.987	6.00×10^{-4}	090417B	…	…
060522	…	…	090418A	0.367	9.58×10^{-1}
060526	…	…	090423	…	…
060602A	…	…	090424	0.740	2.81×10^{-3}
060605	0.528	1.43×10^{-1}	090429B	…	…
060607	…	…	090618	0.260	5.36×10^{-3}
060614	0.459	7.85×10^{-4}	090709A	0.461	1.87×10^{-2}
060719	0.581	1.07×10^{-1}	091127	0.833	9.62×10^{-3}
060729	0.246	1.60×10^{-2}	091208B	…	…
060912A	0.525	4.31×10^{-2}	100205A	…	…
060923A	0.980	3.49×10^{-3}	100316D	0.879	…
060927	…	…	100413A	…	…
061007	0.778	7.67×10^{-2}	100526A	0.531	6.43×10^{-2}
061110A	0.419	4.59×10^{-2}	100615A	0.051	14.8
061110B	0.393	6.90×10^{-2}	100621A	0.914	6.51×10^{-2}
061222A	0.955	4.92×10^{-2}	100905A	…	…
070125	…	…	110312A	…	…
070208	0.928	6.91×10^{-3}	110709B	0.055	19.6
070306	0.798	4.29×10^{-2}	110731A	0.029	2.53×10^{-3}
070318	0.781	7.85×10^{-2}	111215A	0.012	1.89×10^{-1}
070508	0.517	1.83×10^{-3}	120119A	1.000	4.14×10^{-3}
070521	…	…	120711A	0.978	7.26×10^{-4}
070721B	0.211	8.58×10^{-1}	120923A	…	…
070802	0.692	1.30×10^{-2}	130427A	…	2.49×10^{-6}
071010A	0.867	2.04×10^{-1}	130925A	0.852	3.17×10^{-4}
071010B	0.825	7.34×10^{-3}			

the fact that an offset is a positive-definite quantity as described by a Rice distribution. The shift is dominated by the ∼15 LGRBs for which the uncertainty is larger than the offset.

It is important to carefully consider the effects of the uncertainties on the distribution of offsets because offsets with uncertainties that are large relative to the offset itself have probability distributions skewed to larger offset. Given a large uncertainty, the measured offset is more likely to be large due to the large area encompassed by the error circle at large offset. $\sigma_{R_{\rm phys}}$ should not be correlated with the intrinsic offset, so if the true offset distribution extended to small offsets, this effect would cause a bias against finding them when the uncertainties are large. We plot $\sigma_{R_{\rm phys}}$ versus $R_{\rm phys}$ in Figure 6. Of the 11 bursts in the sample with $\sigma_{R_{\rm phys}} \gtrsim 1.0$ kpc, all are at measured offsets $\gtrsim$0.5 kpc, whereas the remaining bursts with $\sigma_{R_{\rm phys}} \lesssim 1.0$ kpc span the full range of offsets from 0.075 to 14 kpc. Because there is no relationship between the true offset and $\sigma_{R_{\rm phys}}$, the range of offsets found with large uncertainty

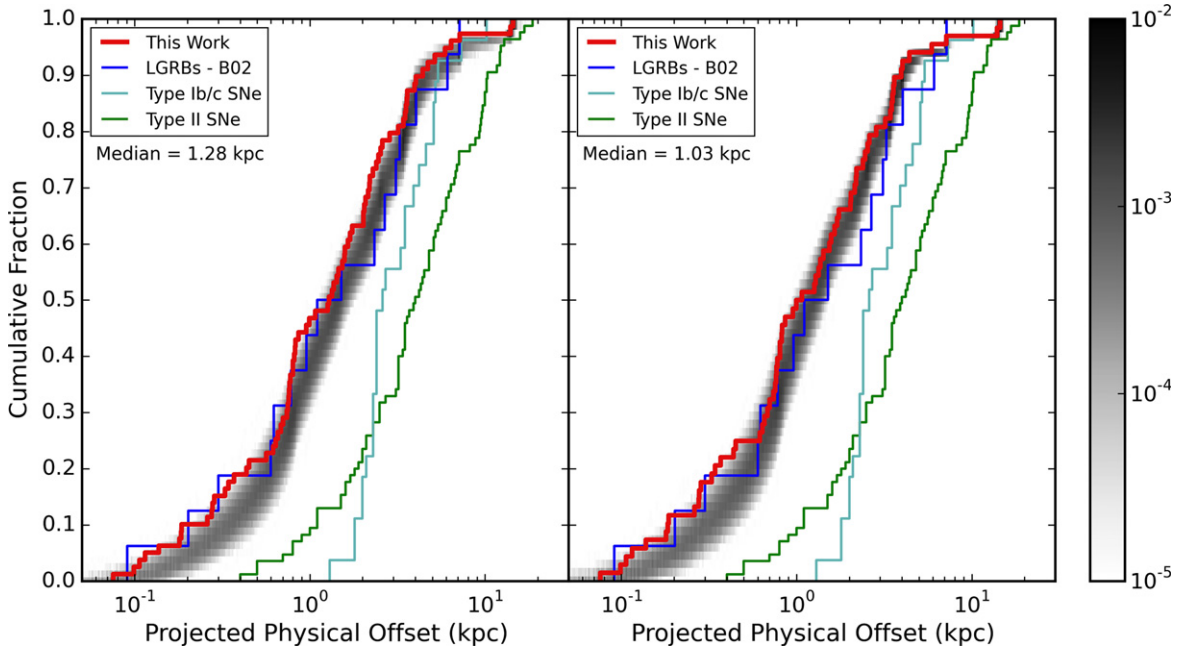

Figure 5. Left: cumulative distributions of the projected physical offsets of 79 LGRBs from this work (red) and Bloom et al. (2002; B02, blue). We also show the distributions for Type Ib/c (cyan) and Type II (green) SNe from Prieto et al. (2008). The shaded region displays the results of our Monte Carlo assessment of the uncertainties on the offsets in the form of a 2D histogram. Right: similar to the left panel, except here we plot the sample of 68 bursts with $\sigma_{R_{\rm phys}} \lesssim 1.0$ kpc to reduce any bias caused by bursts with a large offset uncertainty (see Figure 6). The results are essentially unchanged.

should not be significantly different from the range found with small uncertainty. The fact that we only measure large offsets when we have large uncertainty is indicative of the aforementioned bias. We note that even at relatively small uncertainty we may still be missing bursts at very small offsets because any amount of uncertainty prevents the measurement of arbitrarily small offsets.

To reduce this bias, we make a quality cut on our physical offset sample by also plotting in Figure 5 the distribution for bursts with $\sigma_{R_{\rm phys}} \lesssim 1.0$ kpc, which tightens our sample to 68 LGRBs. The resulting distribution has a median at 1.03 kpc. The mean of the distribution of medians for each iteration of the Monte Carlo simulation is 1.20 kpc with a 90% confidence interval of 1.03–1.37 kpc. In comparison to the sample of Bloom et al. (2002), a KS and AD test yields p-values of 0.80 and 0.82, respectively.

We also compare the distribution of projected physical offsets to the distributions for Type II and Ib/c SNe. KS tests with the supernovae samples of Prieto et al. (2008) yield p-values of 2.0×10^{-7} and 2.1×10^{-8} for the Type Ib/c and II SNe, respectively. AD tests yield 2.6×10^{-5} and 4.2×10^{-5}, respectively. LGRBs occur significantly closer to the centers of their host galaxies in a physical sense than SNe. To disentangle the effects of galaxy size differences between LGRB hosts and SNe hosts, we revisit supernova comparisons in the next section where we analyze the LGRB host-normalized offsets.

4.1.2. Host-normalized Offset Distribution

Normalizing the offsets by the host galaxy sizes enables a fair comparison across the LGRB sample and with the SNe samples. In Figure 7 we plot the cumulative distribution of host-normalized offsets (R/R_h). The distribution ranges from about 0.04 to 7.0. The median of the distribution is 0.59, and about 90% of the bursts occur within a host-normalized offset of $\approx$2.2. Overall, the distribution is reminiscent of an exponential disk profile, the expected surface brightness profile of star-forming disk galaxies. For comparison, we also plot the predicted distribution of host-normalized offsets if LGRB locations exactly trace an exponential disk profile. Although the shapes are overall consistent between our measured distribution and that of an exponential disk, there is a notable shift to lower offsets seen in our distribution. Again, to compare with the previous offset sample of LGRBs, we show the host-normalized offsets from Bloom et al. (2002). KS and AD tests between this sample and our sample yield p-values of 0.25 and 0.20, respectively. As a result of the small sample size, Bloom et al. (2002) concluded that the LGRB host-normalized offsets were consistent with being drawn from the exponential disk profile. With our larger sample we can rule this out at a significance level of 2.8×10^{-5}. Given the irregular morphologies of LGRB host galaxies this result is not surprising, even if LGRBs trace star formation.

As with the physical offsets, we also show the uncertainty region determined from our Monte Carlo procedure in Figure 7. Again, we carefully consider the effects of the uncertainties on the distribution of the host-normalized offsets to avoid the aforementioned bias associated with the offset measurement of bursts with large offset uncertainties. In Figure 6, we also plot $\sigma_{R_{\rm norm}}$ versus $R_{\rm norm}$. Of the 14 bursts in the sample with $\sigma_{R_{\rm norm}} \gtrsim 0.5$, all are at measured offsets $\gtrsim$0.4, whereas the remaining bursts with $\sigma_{R_{\rm norm}} \lesssim 0.5$ span the full range of offsets from 0.04 to 7.0. As with the physical offsets, our inability to measure small offsets when we have large uncertainty is indicative of a bias. Again, it is likely that even at relatively small uncertainty we may still be missing bursts at very small offsets.

As before, we make a quality cut on our host-normalized offset sample by restricting the sample to bursts with

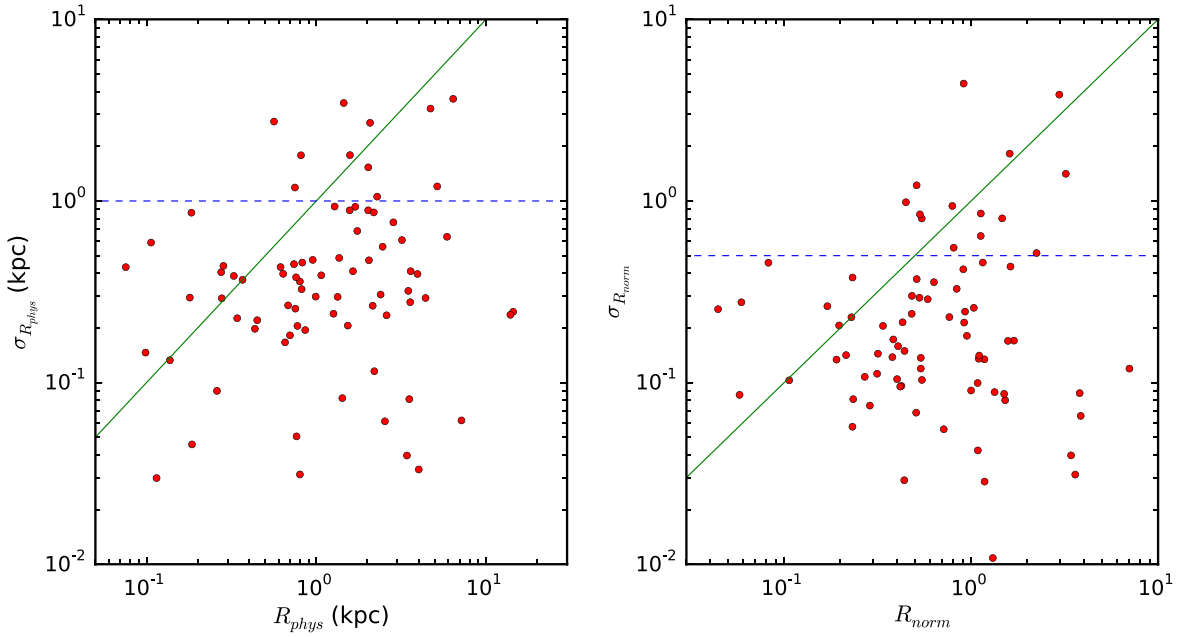

Figure 6. Left: uncertainty in physical offset ($\sigma_{R_{\rm phys}}$) vs. physical offset ($R_{\rm phys}$). The green line marks $\sigma_{R_{\rm phys}} = R_{\rm phys}$. Right: uncertainty in host-normalized offset ($\sigma_{R_{\rm norm}}$) vs. host-normalized offset ($R_{\rm norm}$). Similarly, the green line marks $\sigma_{R_{\rm norm}} = R_{\rm norm}$. Because $\sigma_{R_{\rm norm}}$ and $\sigma_{R_{\rm phys}}$ are not related to the intrinsic offset, the apparent lack of small offsets with large uncertainty (the gap in the upper left quadrant of both plots) is indicative of a bias to large offset associated with bursts that have poor localizations. The dashed blue lines at $\sigma_{R_{\rm phys}} = 1$ kpc and $\sigma_{R_{\rm norm}} = 0.5$ mark the locations of our cuts.

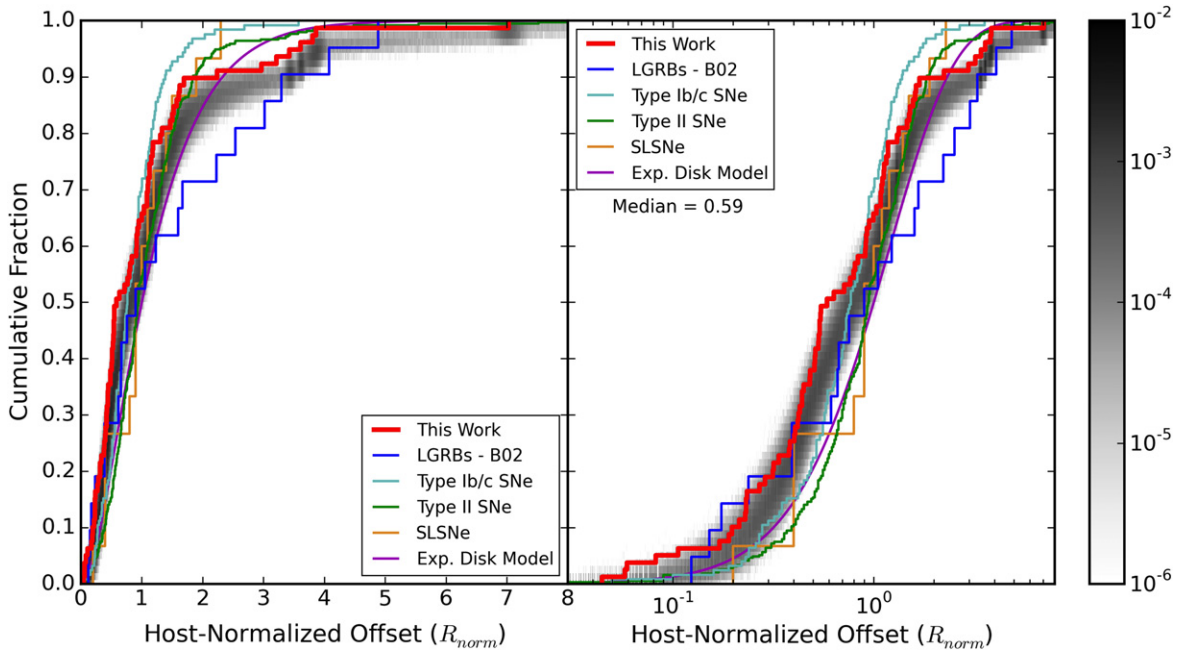

Figure 7. Cumulative distributions of LGRB host-normalized offsets for our sample (red) and the sample of Bloom et al. (2002; B02, blue) shown on linear (left) and log (right) x-axis scales. Also shown are the distributions for Type Ib/c (cyan) and Type II (green) SNe from Kelly & Kirshner (2012) and SLSNe (orange) from Lunnan et al. (2015). We also plot the distribution expected for an exponential disk profile (magenta). The shaded regions depict the uncertainties on our offset measurements determined using a Monte Carlo simulation. We find an offset distribution that is qualitatively similar in shape to an exponential disk profile, but statistically inconsistent.

$\sigma_{R_{\rm norm}} \lesssim 0.5$, resulting in a sample of 65 LGRBs. The resulting distribution has a median at 0.54. In Figure 8, we show the individual probability distributions of each LGRB used in the Monte Carlo simulation. The mean of the distribution of medians for each iteration of the Monte Carlo simulation is 0.63 with a 90% confidence interval of 0.55–0.72. We plot the distribution and Monte Carlo results in Figure 9. A KS test with the exponential disk model yields a p-value of 6.2×10^{-6}. Furthermore, only ∼0.02% of the Monte Carlo synthetic distributions have p-values >0.05 when compared to an exponential disk profile, meaning that we can rule out the hypothesis that LGRB host-normalized offsets are drawn from an exponential disk. As another way to view these results, we also show the sum of the individual probability distributions of

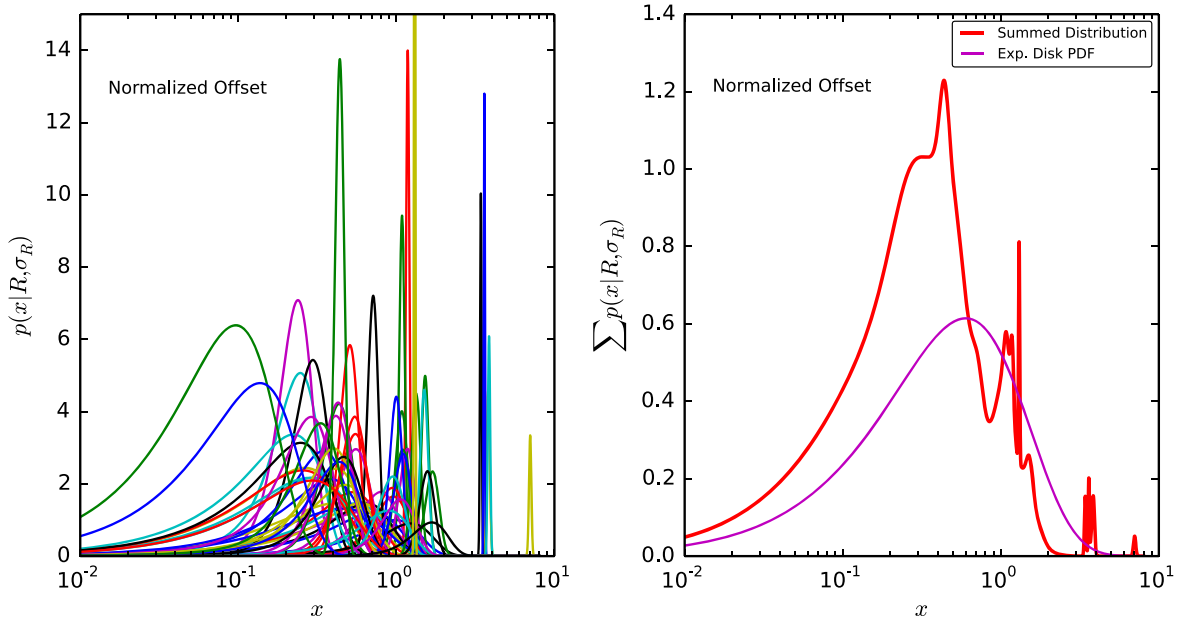

Figure 8. Left: probability distributions for each LGRB with $\sigma_{R_{\rm norm}} \lesssim 0.5$ given its measured offset and offset uncertainty calculated using Equation (2). Narrow peaks indicate well-localized bursts while broader distributions indicate poorer localizations. Right: sum (red) of the individual probability distributions (left) effectively producing a smoothed histogram of the offsets. In magenta we show the probability distribution for an exponential disk. The summed distribution is clearly offset to lower offsets than what would be expected for a population tracing an exponential disk.

each LGRB in Figure 8. The summed distribution effectively produces a smoothed histogram of the offsets and shows a clear shift to smaller offsets from the probability distribution for an exponential disk profile. LGRBs are apparently highly concentrated in the inner parts of their hosts. In particular, they are more concentrated than the radial light distributions of their hosts; namely, 50% of LGRBs occur within 63% of a half-light radius. Stated differently, about half of all LGRBs occur within a region that contains only 32% of the underlying distribution of light in their host galaxies. The aforementioned possible bias caused by the inability to find bursts at very small offsets would act contrary to the striking result found here, indicating that the distribution may be even more concentrated.

A striking feature of the distribution in Figure 9 is the apparent tail to large offset extending from a gap at $R_{\rm norm} \sim 1.6$–3.3. While it is not unexpected, given the rough similarity of our distribution to an exponential disk, to find bursts at large offset, it is somewhat surprising that ∼10% of LGRBs appear to be located at $R_{\rm norm} \gtrsim 3$. These bursts include GRBs 050820, 081008, 080928, 060418, and 060505. We revisit the properties of these bursts and their assigned hosts. The host of GRB 050820 has a morphology consisting of a bright core with a diffuse tail, with the GRB located on this diffuse emission, leading to a host-normalized offset of 3.8 from the bright core. The burst's location on the underlying galaxy emission and the $P_{\rm cc}$ of 0.009 do not give reason to doubt the host association, with the large offset being due to the unusual morphology. As discussed in Section 3.3.1, we assigned as the host of GRB 080928 a non-coincident galaxy with a luminosity consistent with the observed distribution of LGRB host luminosities. However, we cannot rule out the possibility that the host was not detected and that the assigned candidate is instead the source of an intervening absorption system observed in the afterglow (Vreeswijk et al. 2008), casting doubt on the large inferred offset. GRB 081008, another burst with a host assigned based on our luminosity analysis, has a large normalized offset of ≈7 and $P_{\rm cc} \approx 0.07$. While the host assignment matches our criteria, we acknowledge the possibility that the assignment is not correct. For GRB 060418, we assign as the host the brighter of the two nearby host components identified by Pollack et al. (2009). Although these components are distinct from each other (see Figure 2), the assignment of one or the other has little effect on the offset and no effect on the fractional flux. GRB 060505 is a controversial $z = 0.089$ burst that did not have an associated supernova, as expected for a low-z LGRB, leading some to argue in favor of a short GRB scenario (Ofek et al. 2007). However, given its location in a bright, low metallicity H II region of its host, others argue in favor of 060505 as a LGRB (Thöne et al. 2014). In this case, 060505 is an example of a LGRB occurring at large normalized offset (3.6) and at high fractional flux (0.99) in the outskirts of its host. It is interesting to speculate that the other bursts at large offsets may be higher redshift versions of 060505 where underlying H II regions are too faint to be detected. For the reasons discussed here, the large offset tail in the distribution of host-normalized offsets may not be real. However, it does not affect the overall conclusion that LGRBs as a population are more centrally concentrated than the underlying light distributions of their hosts.

We compare our distribution of LGRB host-normalized offsets with those measured for supernovae by Kelly & Kirshner (2012), also shown in Figure 9. KS tests with the Type Ib/c and Type II SNe yield p-values of 2.4×10^{-3} and 1.2×10^{-6}, respectively. AD tests yield p-values of 5.7×10^{-3} and 2.6×10^{-5}, respectively. About 45% of Monte Carlo synthetic distributions have p-values >0.05 when compared to Type Ib/c SNe using a KS test. This percentage is 42% when using the AD test. While the distributions for LGRBs and Type Ib/c SNe appear to be statistically inconsistent, it is interesting that both are more centrally concentrated than Type II SNe and the exponential disk profile.

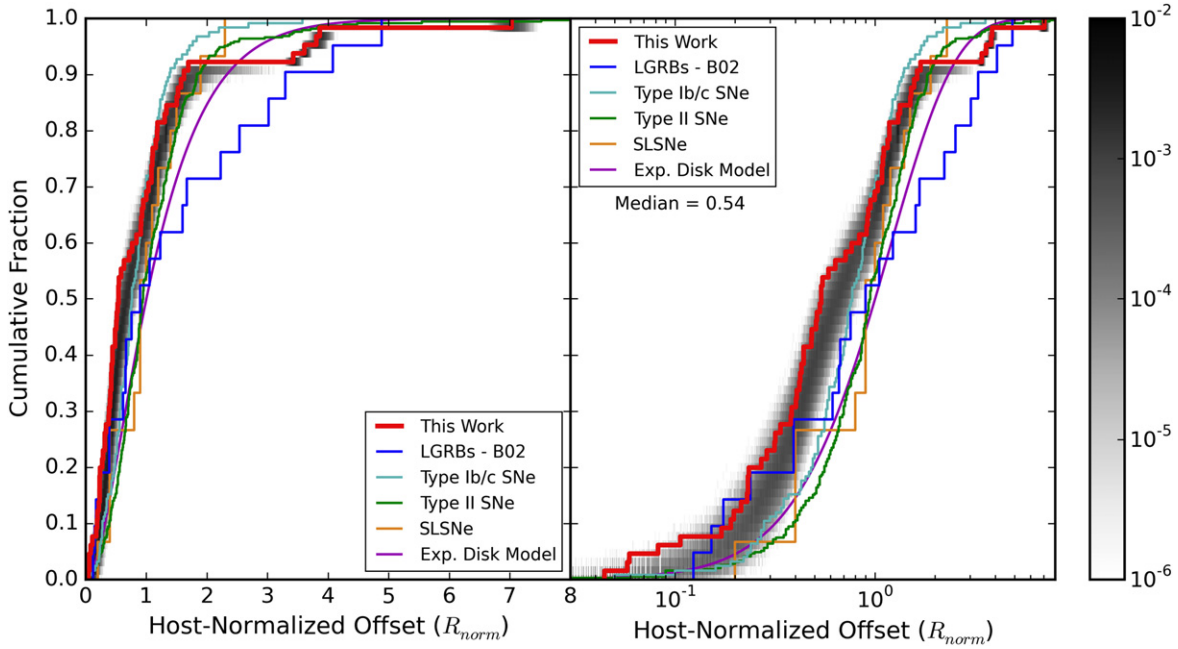

Figure 9. Similar to Figure 7, except here we show the distribution of host-normalized offsets for bursts with $\sigma_{R_{\rm norm}} \lesssim 0.5$. The distribution is shifted to lower offsets with a median of 0.54. This is because we removed bursts with large offset uncertainties that bias the distribution to larger offsets (see Figure 6).

To better visualize the comparison between LGRBs and supernovae and each with the exponential disk, we plot in Figure 10 the ratios of each transient's cumulative offset distribution to the exponential disk distribution. The plot illustrates that none of these transients follow an exponential disk profile and that LGRBs differ significantly from supernovae in their relationship to the exponential disk. At nearly all offsets, LGRBs show an overabundance in a cumulative sense with respect to the exponential disk, whereas the supernovae exhibit an oscillatory pattern. In particular, the Type II SNe show a substantial deficit with respect to the exponential disk up until an offset of ∼0.9, beyond which they exhibit an overabundance. In stark contrast to the LGRBs, Type Ib/c and II SNe occur infrequently near the centers of their host galaxies. Though Type Ib/c SNe seem to avoid their host centers, they also avoid offsets larger than ∼1.5, seeming to prefer a band of offsets near the half-light radius. Comparing our LGRBs to the distribution measured for super-luminous supernovae (SLSNe; Lunnan et al. 2015) we find KS and AD test p-values of 0.10 and 0.21, respectively. This comparison, though, is limited by the small SLSNe sample size.

4.1.3. Offset Distribution Summary

We find that our sample of LGRBs spans the range 0.075 to 14.4 kpc (mean of Monte Carlo distribution of medians = 1.20 kpc) in physical offset from the centers of their host galaxies. When appropriately accounting for uncertainties and removing bursts with $\sigma_{R_{\rm norm}} \gtrsim 0.5$, we find that LGRB host-normalized offsets are considerably smaller and more centrally concentrated (mean of Monte Carlo distribution of medians = 0.63, with a 90% confidence interval of 0.55–0.72) than what would be expected if LGRBs traced an exponential disk profile. We can rule out at high significance that LGRB offsets are drawn from an exponential disk distribution and their distribution is inconsistent with both Type II and Type Ib/c SNe. LGRBs prefer the central locations in their hosts, because they are more concentrated than the underlying host light distributions. Tables 4 and 5 provide a summary of the KS and AD p-values, respectively, that we find for comparisons between our sample of LGRB host-normalized offsets and other types of stellar explosions; Table 6 shows the distribution statistics.

4.2. Host Light Distribution

In Figure 11 we show the cumulative distribution of the fractional flux for the 57 bursts in our sample that have error circle to galaxy area ratios of $\lesssim$0.1 (left panel). Ideally, we would like to assess whether or not LGRBs are spatially coincident with bright rest-frame UV regions of their hosts, which trace young, massive stars. As shown in Figure 1, our observations primarily probe the rest-frame optical emission, which may probe older stellar populations. Here, we compare the fractional flux distribution for the ∼20% of the sample that probes rest-frame UV to the distribution that probes the rest-frame optical. The right panel of Figure 11 shows the resulting distributions when dividing the sample by wavelength into two bins separated at $\lambda_{\rm rest} = 5000$ Å. The rest-frame optical and blue/UV distributions agree well, which we interpret as indicating that there is no bias in using rest-frame optical observations as a proxy for rest-frame UV. If there was a separate older stellar population, we would not expect to find LGRB positions correlated so strongly with both the optical and UV light. In other words, the optical and UV light are probing the same population of stars. We can then interpret our fractional flux measurements as reflecting the relationship between location and the host UV emission.

As shown in Figure 11, the fractional flux distribution for our sample spans the full range from 0 to 1 with 90% of values falling in the range 0.03–0.98. The median is 0.78 and nearly 80% of bursts have fractional flux values greater than 0.5. This strong preference toward higher fractional flux values indicates that LGRBs are typically located on some of the brightest regions of their hosts, and lends further support to the idea that

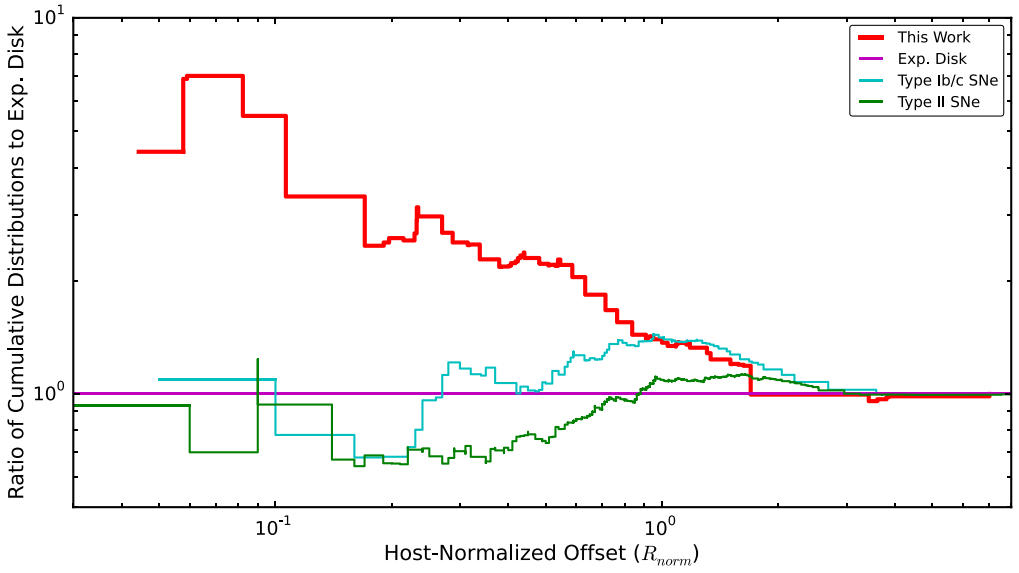

Figure 10. Ratios of the cumulative host-normalized offset distributions of our sample, Type Ib/c SNe, and Type II SNe to the cumulative distribution for an exponential disk. In other words, the ratios of the distributions in Figure 9 to the magenta curve. The spikes in the supernovae curves are caused by multiple objects with the same offset, corresponding to large steps in the cumulative distributions. This plot illustrates the differences between these distributions and the exponential disk, clearly showing the deficit of supernovae at small offset, in stark contrast to LGRBs.

Table 4
Summary of Kolmogorov–Smirnov (KS) Test *p*-values

LGRBs—This Work	Exp. Disk	Type Ib/c SNe[a]	Type Ic SNe	Type II SNe	CCSNe	SLSNe	LGRBs–F06	LGRBs–B02
Physical Offsets	…	2.0×10^{-7}	…	2.1×10^{-8}	…	…	…	0.80
Host-Normalized Offsets	6.2×10^{-6}	2.4×10^{-3}	…	1.2×10^{-6}	…	0.10	…	0.16
Fractional Fluxes	…	…	0.82	3.0×10^{-6}	4.2×10^{-3}	0.33	0.24	…

Note. The values reported here for the physical offsets, host-normalized offsets, and fractional fluxes include only bursts with $\sigma_{R_{\rm phys}} \lesssim 1.0$ kpc, $\sigma_{R_{\rm norm}} \lesssim 0.5$, and error circle to galaxy area ratio $\lesssim$0.1, respectively. Comparison samples of Type Ib/c and II SNe (physical offsets), Type Ib/c and II SNe (host-normalized offsets), Type Ic and II SNe (fractional fluxes), CCSNe, SLSNe, LGRBs—F06, and LGRBs—B02 are from Prieto et al. (2008), Kelly & Kirshner (2012), Kelly et al. (2008), Svensson et al. (2010), Lunnan et al. (2015), Fruchter et al. (2006), and Bloom et al. (2002), respectively.
[a] For the host-normalized offsets, 45% of LGRB Monte Carlo synthetic distributions have *p*-values >0.05 when compared to Type Ib/c SNe.

Table 5
Summary of Anderson–Darling (AD) Test *p*-values

LGRBs—This Work	Exp. Disk	Type Ib/c SNe[a]	Type Ic SNe	Type II SNe	CCSNe	SLSNe	LGRBs—F06	LGRBs—B02
Physical Offsets	…	2.6×10^{-5}	…	4.2×10^{-5}	…	…	…	0.82
Host-Normalized Offsets	…	5.7×10^{-3}	…	2.6×10^{-5}	…	0.21	…	0.11
Fractional Fluxes	…	…	0.95	2.3×10^{-5}	3.1×10^{-3}	0.56	0.05	…

Note. See notes for Table 4.
[a] For the host-normalized offsets, 42% of LGRB Monte Carlo synthetic distributions have *p*-values >0.05 when compared to Type Ib/c SNe.

LGRBs originate from very massive stars. This is in broad agreement with previous claims (Fruchter et al. 2006; Svensson et al. 2010). In Figure 11 we also show the distribution of fractional flux for the sample of 30 LGRBs from Fruchter et al. (2006). A KS test between the two samples yields a *p*-value of 0.24, while an AD test yields a *p*-value of 0.05. This indicates that while our sample and the Fruchter et al. (2006) sample are marginally inconsistent, we cannot rule out that they are drawn from the same distribution. Nevertheless, the sample of Fruchter et al. (2006) has a higher median and general inclination toward higher fractional flux values. This slight discrepancy is probably not caused by effects intrinsic to the LGRB population, but rather by systematic differences between the two samples. We also show the Fruchter et al. (2006)

Table 6
Summary of LGRB Offset and Fractional Flux Statistics

	Sample Median	Mean[a]	90% Confidence Interval
Physical Offsets	1.03 kpc	1.20 kpc	1.03–1.37 kpc
Host-Normalized Offsets	0.54	0.63	0.55–0.72
Fractional Fluxes	0.78	…	…

Note. The values reported here for the physical offsets, host-normalized offsets, and fractional fluxes include only bursts with $\sigma_{R_{\rm phys}} \lesssim 1.0$ kpc, $\sigma_{R_{\rm norm}} \lesssim 0.5$, and the error circle to galaxy area ratio $\lesssim$0.1, respectively.
[a] Estimated from the distribution of medians of the synthetic distributions produced by the Monte Carlo simulation.

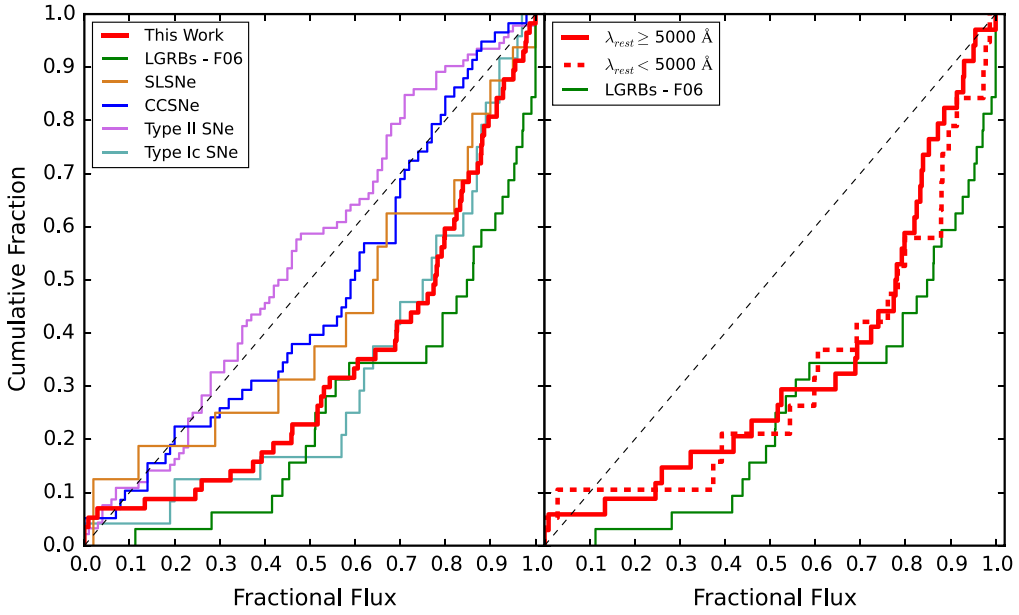

Figure 11. Left: cumulative distributions of fractional flux for our sample (red), the LGRB sample of Fruchter et al. (2006; F06, green), CCSNe from Svensson et al. (2010; blue), SLSNe from Lunnan et al. (2015; orange), and Type Ic (cyan) and II (violet) SNe from Kelly et al. (2008). We only include bursts in our sample with a ratio of error circle to galaxy area of $\lesssim$0.1 (Figure 4). The diagonal dashed line shows the expected fractional flux distribution for a population uniformly tracing the underlying light of their host galaxies. Right: cumulative distributions of fractional flux for two subsets of the sample divided at a rest-frame wavelength of 5000 Å. The agreement between the two means that we can use the rest-frame optical observations as a proxy for rest-frame UV.

sample with the wavelength binned distributions in Figure 11. Due to the fact that the Fruchter et al. (2006) sample comprises mostly rest-frame UV observations, one might consider that the discrepancy is the result of a bandpass difference between the two samples. However, the agreement of the rest-frame optical and blue/UV distributions indicates that the discrepancy is likely not a bandpass effect. We address another potential effect in Section 5.

We also compare our measured distribution to the corresponding distributions measured for CCSNe (Svensson et al. 2010), SLSNe (Lunnan et al. 2015), and Type Ic and II SNe (Kelly et al. 2008). KS tests among our sample, the SLSNe sample, the Type Ic SNe sample, the Type II SNe sample, and the CCSNe sample yield p-values of 0.33, 0.82, 3.0×10^{-6}, and 4.2×10^{-3}, respectively. AD tests yield p-values of 0.56, 0.95, 2.3×10^{-5}, and 3.1×10^{-3}, respectively. We cannot rule out that our sample of LGRBs and the SLSNe sample are drawn from the same distribution. Interestingly, our sample overlaps the SLSNe distribution at fractional flux values of $\gtrsim$0.8. The very good agreement between the distributions for our sample and the Ic SNe sample is consistent with the fact that Ic SNe, particularly Ic-BL, is the only type of SNe observed to be associated with LGRBs. The distributions of fractional flux for the CCSNe, mostly consisting of Type II SNe, and the Type II SNe sample are clearly distinct from our LGRB distribution, which is strong evidence that Type II SNe and LGRBs have different progenitors. We summarize the KS and AD p-values for our comparisons in Tables 4 and 5, respectively.

4.3. Galaxy Sizes

As it pertains to our knowledge of the host galaxies and therefore implications for the progenitors, we plot in Figure 12 the cumulative distribution of 80% light radii (R_{80}) of our host galaxies. The median size for the LGRB sample is 3.0 kpc and the distribution spans from $R_{80} \sim 0.6$ kpc to $R_{80} \sim 10$ kpc. For comparison, we show the distributions for the samples of LGRBs and CCSNe studied by Svensson et al. (2010). An AD test reveals that our distribution, though shifted to slightly higher values of R_{80}, is consistent with their distribution of LGRB sizes. A KS and AD test between our distribution of LGRB sizes and the CCSNe distribution yields p-values of 2.3×10^{-3} and 6.3×10^{-4}, respectively, indicating that our larger sample of LGRBs is in full agreement with the conclusion of Svensson et al. (2010) that LGRB host galaxies are on average smaller than CCSNe host galaxies. Figure 12 also shows the sample of SLSNe host galaxies studied by Lunnan et al. (2015). With the previous small sample of LGRBs, the SLSNe and LGRB host size distributions were statistically consistent. Now, with our larger sample we find that the apparent larger sizes of LGRB hosts are statistically robust (KS p-value $= 1.3 \times 10^{-3}$, AD p-value $= 8.2 \times 10^{-4}$).

4.4. Durations and Energies

The durations (as measured by T_{90}) and isotropic equivalent energies ($E_{\gamma,\rm iso}$) of LGRBs each vary by more than several orders of magnitude. Whether or not environmental factors influence these variations in burst properties is an open question that we can address with our sample of offsets and fractional fluxes. In Figure 13 we plot fractional flux and host-normalized offsets versus T_{90} and $E_{\gamma,\rm iso}$. We find no significant correlations between the fractional flux or offset with T_{90} or $E_{\gamma,\rm iso}$, indicating that the locations of LGRBs within their host galaxies do not affect the properties of the bursts themselves. Our findings do not support the claim of a possible trend between host-normalized offset and isotropic equivalent energy reported by Ramirez-Ruiz et al. (2002) based on a much smaller sample of 16 pre-*Swift* events.

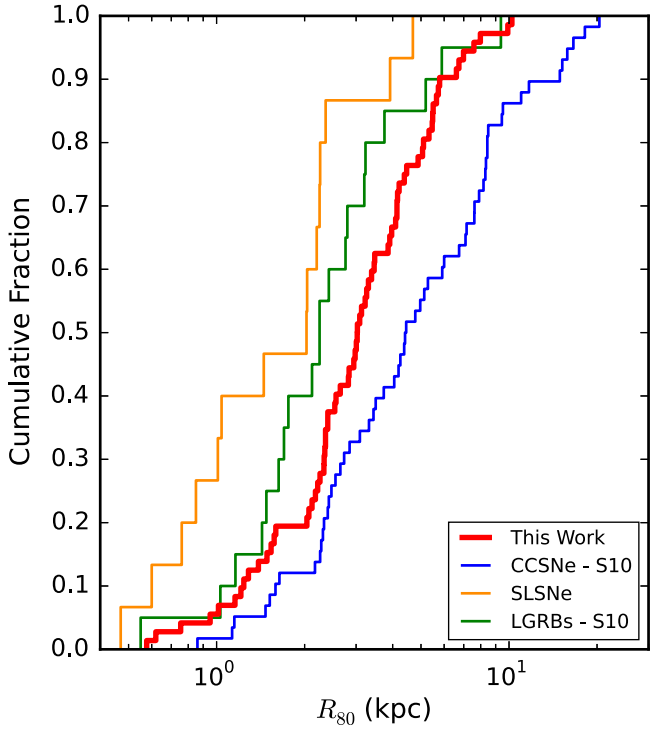

Figure 12. Cumulative distributions of R_{80} for our sample of LGRBs (red), the LGRB (green) and CCSNe (blue) samples from Svensson et al. (2010; S10), and the SLSNe sample from Lunnan et al. (2015; orange). At high significance we find that LGRB host galaxy sizes are larger than SLSNe host sizes but smaller than CCSNe host sizes.

5. DISCUSSION

The distributions of offsets and fractional flux presented in Section 4 provide the most in-depth look at the locations and environments of LGRBs presented to date. Furthermore, our sample is sufficiently large and wide in redshift to allow the investigation of trends with cosmic time. Here we discuss possible redshift evolution, the relationship between fractional flux and host-normalized offset, and the implications for the progenitors of LGRBs provided by this new view of their locations.

5.1. Redshift Trends

In Figure 14 we show the physical offsets for bursts with $\sigma_{R_{\rm phys}} \lesssim 1.0$ kpc as a function of redshift (right panel) and the cumulative distribution of physical offsets binned into three equally populated bins of redshift (left panel): $z \leqslant 0.9$, $0.9 < z \leqslant 1.8$, and $z > 1.8$. We find that there is no statistically significant trend of the physical offsets as a function of redshift. KS tests between the three redshift bins yield p-values of 0.82, 0.62, and 0.86 for the low-z and mid-z bins, low-z and high-z bins, and mid-z and high-z bins, respectively. AD tests yield p-values of 0.95, 0.66, and 0.77, respectively.

In Figure 15 we show the host-normalized offsets of bursts with $\sigma_{R_{\rm norm}} \lesssim 0.5$ as a function of redshift (right panel) and the cumulative distribution of host-normalized offsets binned by redshift (left panel). Overall we find no significant trend of the host-normalized offsets with redshift. KS tests between the three redshift bins yield p-values of 0.56, 0.96, and 0.41 for the low-z and mid-z bins, low-z and high-z bins, and mid-z and high-z bins, respectively. AD tests yield p-values of 0.47, 0.76, and 0.38, respectively.

In Figure 16 we show the fractional flux distribution binned into the same three redshift bins. KS tests between the three redshift bins yield p-values of 0.95, 0.41, and 0.77 for the low-z and mid-z bins, low-z and high-z bins, and mid-z and high-z bins, respectively. AD tests yield p-values of 0.83, 0.45, and 0.83, respectively. There is no statistically significant trend of fractional flux with redshift.

Overall we find no statistically significant trends with redshift in the offset or fractional flux distributions.

5.2. The Fractional Flux–Offset Relationship

In Figure 17 we plot the fractional flux versus host-normalized offset for bursts satisfying the error circle area to galaxy area ratio of $\lesssim$0.1 and $\sigma_{R_{\rm norm}} \lesssim 0.5$. We find a clear correlation between fractional flux and host-normalized offset, where bursts at smaller offsets have high fractional flux values and bursts at larger offsets have on average lower fractional flux values. The scatter in the fractional flux values increases with increasing $R_{\rm norm}$. All bursts in our sample with $R_{\rm norm} \lesssim 0.5$ have fractional flux values greater than 0.6, yielding a notable lack of bursts with small offsets and low fractional flux values. Beyond $R_{\rm norm} \approx 0.5$, the fractional flux values are on average lower, but also show considerable scatter. Bursts with $R_{\rm norm} \gtrsim 1$ have fractional flux values spanning the full range from zero to one.

While it is not surprising that a trend should exist between fractional flux and offset given that regions close to the centers of galaxies are brighter, the coupling of fractional flux and offset information explains the results seen in the fractional flux distribution. To illustrate this, we also show the cumulative distributions of fractional flux for the subsamples with $R_{\rm norm} \leqslant 0.5$ and $R_{\rm norm} > 0.5$ in Figure 17. Bursts with $R_{\rm norm} \leqslant 0.5$ exclusively occur in regions of high fractional flux and bursts with $R_{\rm norm} > 0.5$ show no preference for unusually bright regions. This means that the shift to high fractional flux we find in the total distribution is entirely due to LGRBs at small offsets and not to bursts at large offset that happen to reside in bright star-forming regions. This observation highlights the fact that solely relying on the fractional flux distribution to make statements about LGRB locations does not capture the full picture. Clearly LGRBs prefer bright star-forming regions in their host galaxies. The offsets show that the central bright region is predominantly preferred. Therefore, it is not simply the presence of a bright star-forming region that affects LGRB production, but rather another factor playing a role near the centers of galaxies must be at play.

Previous studies indicated that the agreement between LGRB offsets and the exponential disk was inconsistent with the observation that LGRBs were highly correlated with the brightest regions of their hosts (Bloom et al. 2002; Fruchter et al. 2006). The offset distribution we measure, coupled with the cumulative distribution of fractional flux showing a preference for bright regions, does not imply a discrepancy. Indeed, the fact that we find LGRBs concentrated in the inner regions of their galaxies with corresponding high fractional fluxes can be interpreted as a relief of the tension between the conclusions of Bloom et al. (2002) and Fruchter et al. (2006). Ultimately, the slight difference between our distribution of fractional flux and the distribution of Fruchter et al. (2006) may be explained by a difference in the offset distributions of the

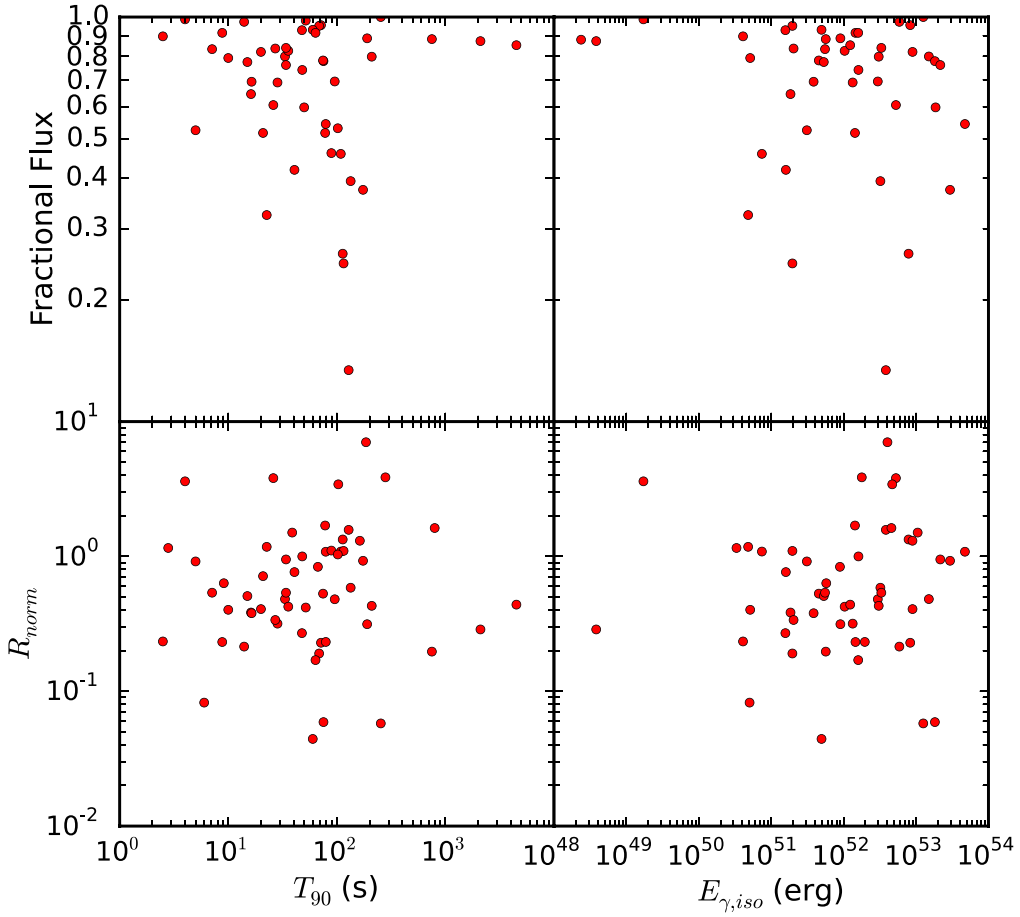

Figure 13. Scatter plots of fractional flux and host-normalized offset ($R_{\rm norm}$) vs. duration (T_{90}) and equivalent isotropic energy ($E_{\gamma,\rm iso}$). We find no significant correlations between these quantities.

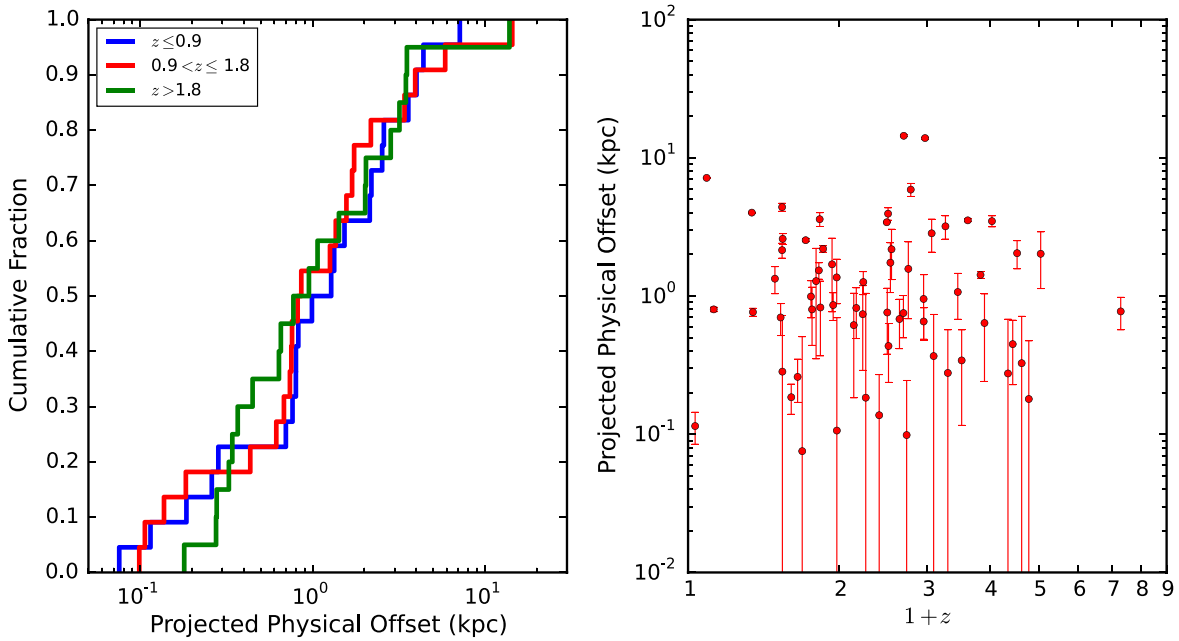

Figure 14. Left: cumulative distribution of physical offsets for bursts with $\sigma_{R_{\rm phys}} \lesssim 1.0$ kpc binned into three equal-numbered bins of redshift: $z \leqslant 0.9$ (blue), $0.9 < z \leqslant 1.8$ (red), and $z > 1.8$ (green). Right: physical offsets with their associated uncertainties as a function of redshift. In both plots we do not include bursts with unknown redshift. We do not find a statistically significant trend in physical offset as a function of redshift.

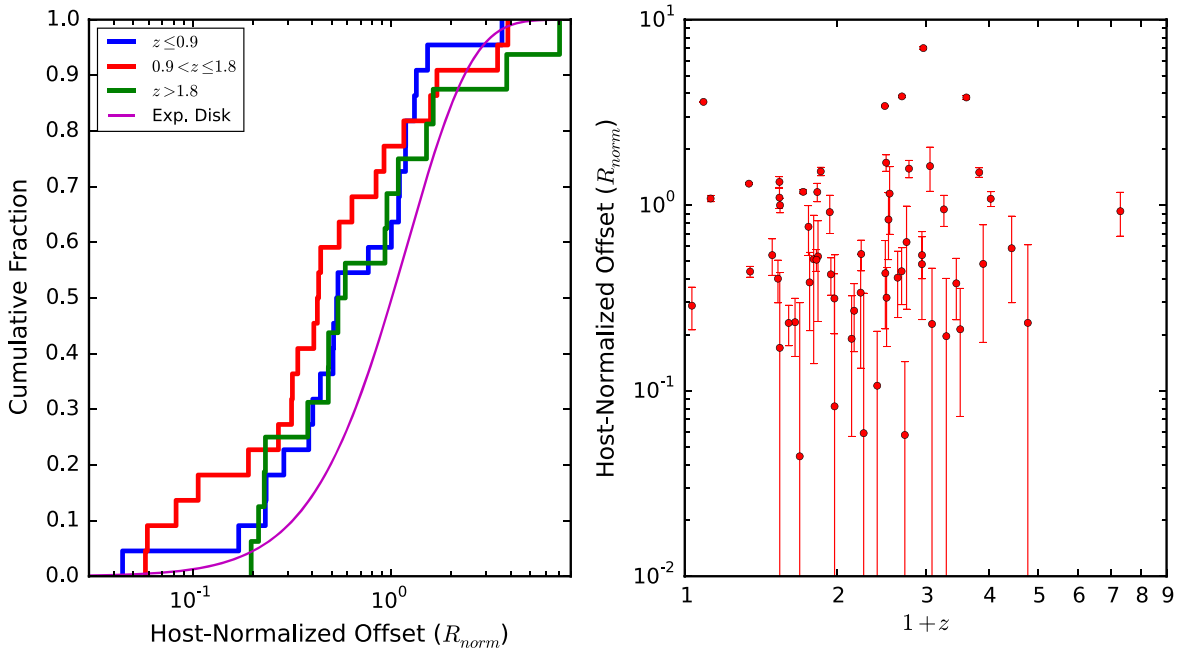

Figure 15. Same as Figure 14 but for the host-normalized offsets of bursts with $\sigma_{R_{\rm norm}} \lesssim 0.5$. We do not find a statistically significant trend in host-normalized offset as a function of redshift.

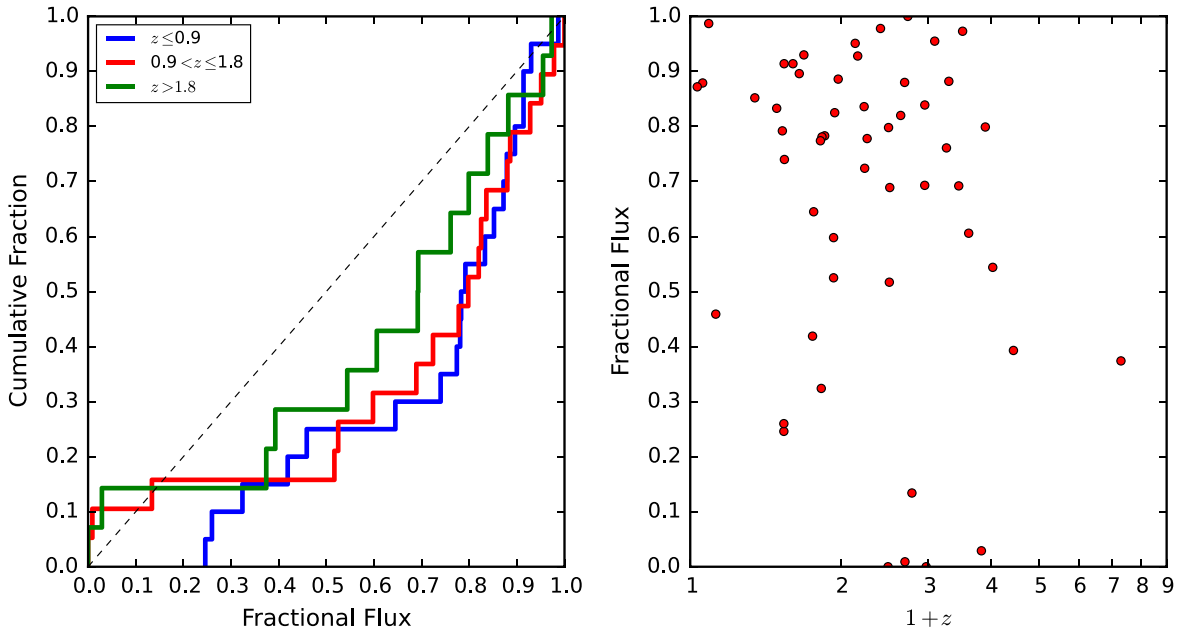

Figure 16. Same as Figure 14 but for fractional flux. We do not find a statistically significant trend in fractional flux as a function of redshift.

two samples, and may simply be the result of small number statistics, where our sample more closely approximates the true underlying distribution.

In Figure 17 we also plot the normalized offsets and fractional fluxes of Type Ic and Ic-BL SNe for objects common to both the sample with fractional fluxes from Kelly et al. (2008) and the sample with host-normalized offsets from Kelly & Kirshner (2012). We find a similar trend between the two quantities. Most of the shift to high fractional flux in the Ic SNe distribution can be attributed to SNe that occurred at small offset. However, Type Ic SNe that occur at $R_{\rm norm} \gtrsim 0.5$ show a slight preference for high fractional fluxes, indicating that at least some of the shift in the full sample is due to a preference for bright regions at large offset.

5.3. Progenitor Implications

We find that LGRBs are on average located at smaller host-normalized offsets than expected for an exponential disk profile of star formation, and are correspondingly more concentrated on brighter regions of their hosts than expected for a population that is simply tracing the underlying light distributions. The evidence presented here suggests that the progenitors of LGRBs prefer the central regions of their hosts, indicating that the properties of star formation toward the inner regions of

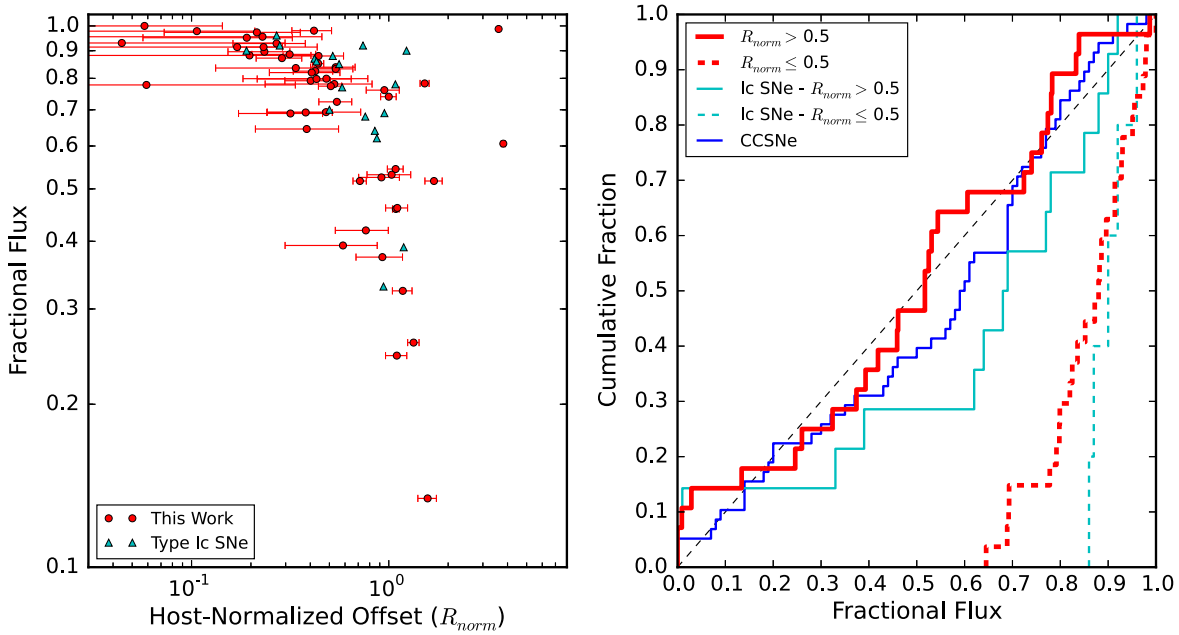

Figure 17. Left: fractional flux vs. host-normalized offset for LGRBs (red) with $\sigma_{R_{\rm norm}} \lesssim 0.5$ and an error circle to galaxy area ratio $\lesssim$0.1 and Type Ic/Ic-BL SNe (cyan) from Kelly et al. (2008) and Kelly & Kirshner (2012). Right: cumulative distributions of fractional flux for two subsets of the LGRB sample divided at $R_{\rm norm} = 0.5$. There is a clear trend relating these two quantities where LGRBs at small host-normalized offset, near the bright cores of their hosts, are exclusively at high fractional flux. At $R_{\rm norm} \gtrsim 0.5$, the bursts show no preference for unusually bright regions similar to CCSNe, as also shown in the right panel. Therefore, the shift to high fractional flux seen in the full sample distribution (Figure 11) is due to bursts occurring in the inner parts of their host galaxies. A similar trend is seen in the Ic SNe sample.

LGRB host galaxies are favorable for LGRB production. As demonstrated in Figure 17, the bursts responsible for the strong preference toward higher fractional flux values are dominated by bursts at small offsets. The fractional flux distribution of bursts at offsets $R_{\rm norm} \gtrsim 0.5$ is a uniform distribution, showing no preference for unusually bright regions. In effect, the high fractional flux values are due to the fact that the bursts occur at small offsets where the host is brighter.

How the suspected metallicity bias of LGRB production fits into this new view of their preferred locations is an important question. Star-forming disk galaxies typically have metallicity gradients with higher metallicities toward the cores (Vila-Costas & Edmunds 1992; Zaritsky et al. 1994). Thus one might expect, if metallicity gradients are also present in the hosts of LGRBs, to more frequently find LGRBs in the outskirts of their hosts, which is contrary to what we find here. Recent resolved studies of low redshift hosts indicate weak metallicity gradients (Levesque et al. 2011; Thöne et al. 2014) and that the global host metallicity is often a sufficient proxy for the metallicity of the burst site. Although the metallicity typically shows only slight variations across the host, the burst site often has the lowest metallicity (Christensen et al. 2008; Levesque et al. 2011; Thöne et al. 2014). In future works, we plan to test for the presence of metallicity gradients, in an average sense, in high redshift hosts by combing ISM metallicity measurements with our measured offsets. While it is clear that metallicity is a factor affecting the production of LGRBs, our results indicate that other factors relating to the mode of star formation may also play a dominant role. The conditions in the central regions of LGRB hosts, perhaps a consequence of their formation histories, may be such that the IMF is different, producing more massive stars and thus more potential LGRB progenitors. It has been shown that massive stars are often found in binary systems (Mason et al. 2009; Sana et al. 2012) and that binary interactions may be important for LGRB production (Fryer et al. 1999; Bromm & Loeb 2006). There may also be increased numbers of massive star binaries in the central regions of LGRB hosts.

The remarkable agreement between the fractional flux distributions of LGRBs and Type Ic SNe corroborates and strengthens the already known common link between their progenitors. While LGRBs and Type Ic SNe broadly prefer similar locations, the exclusive association of LGRBs with Ic-BL SNe indicates that some factor must determine whether a star explodes as a normal Typc Ic, a Type Ic-BL without a LGRB, or a Type Ic-BL with a LGRB. Previous observations suggest that the environments where Type Ic-BL SNe occur are more metal-poor than those for normal Type Ic SNe, and that the environments of Type Ic-BL SNe associated with LGRBs are even more metal-poor (Modjaz et al. 2008, 2011; Kelly & Kirshner 2012). Recent work suggests that metallicity is likely not the only factor influencing the production of Ic-BL SNe and LGRBs. Kelly et al. (2014) found that Ic-BL SNe and LGRBs occur in host galaxies that have higher stellar mass and star-formation rate densities than a control sample of SDSS star-forming galaxies. They show that metallicity cannot explain this preference and instead suggest that another environmental factor—such as increased numbers of young, bound clusters where tight binaries form or a top-heavy IMF—may be at play in Ic-BL SNe and LGRB hosts. The results we find, namely that LGRBs prefer the central regions of their hosts, may be a sub-galactic manifestation of the same environmental factor responsible for the preference for the high global stellar mass and star-formation rate densities seen by Kelly et al. (2014). Whatever this factor is, it seems to influence primarily where LGRBs occur, but not the properties of the explosions themselves, as we do not find correlations between the fractional flux or offset with burst duration or isotropic

equivalent energy. To explain the observed fraction of LGRBs in moderate mass luminous galaxies, another study raised the possibility that other environmental factors beyond metallicity, such as specific star-formation rate, may affect LGRB efficiency (Perley et al. 2015a).

Although the SLSN sample size is much smaller than the LGRB sample size, the statistical consistency between their distributions of fractional flux may be hinting at a connection between these two types of transients. LGRBs and SLSNe arising from similarly bright regions of their hosts would be consistent with a scenario in which the two originated from similar mass progenitors. It could be that in the case of SLSNe, the core is not quite massive enough to form a black hole and instead collapses into a magnetar, while in the case of LGRBs, the core collapses into a black hole (Lunnan et al. 2014). However, the difference in the size distributions of SLSN and LGRB hosts indicates that other factors also influence the production of their progenitors.

6. CONCLUSIONS

We have carried out a comprehensive study of the locations of LGRBs within their host galaxies using *HST* observations of *Swift* bursts compiled over the last decade. Using astrometry from ground- and space-based detections of optical, NIR, radio, and X-ray afterglows, we measure the projected physical and host-normalized offsets of 79 LGRBs from their host centers. In addition, we measure the fractional flux, which allows assessment of the brightness of the burst site relative to the total host light distribution. Upon restricting the sample to avoid biases associated with measurement uncertainty, we obtain sample sizes of 68, 65, and 57 LGRBs for the physical offsets, host-normalized offsets, and fractional fluxes, respectively. These measurements have enabled us to study the offset and fractional flux distributions in great detail, providing an in-depth view into the preferred locations of LGRBs. Our results are as follows:

1. In agreement with previous work (Wainwright et al. 2007), we find that LGRB hosts typically show irregular morphologies and are on average smaller (median = 3.0 kpc) than the host galaxies of CCSNe, although not as small as the hosts of SLSNe.
2. We find that the physical offsets of LGRBs have a mean estimated from the Monte Carlo simulation of 1.20 kpc with a 90% confidence interval of 1.03–1.37 kpc.
3. The host-normalized offsets span a wide range of 0.04 to 7.0 but are concentrated at small values with a mean estimated from the Monte Carlo simulation of 0.63, with a 90% confidence interval of 0.55–0.72. This distribution of LGRB offsets is considerably more concentrated than expected if LGRBs traced an exponential disk (p-value = 6.2×10^{-6}). LGRBs are more concentrated than their host galaxies' own light distributions, such that 50% of bursts reside within a region containing only 32% of the underlying host light.
4. LGRB host-normalized offsets are inconsistent with those of Type II and Ib/c SNe, although both LGRBs and Type Ib/c SNe are more concentrated than Type II SNe.
5. The fractional flux distribution of our sample of LGRBs has a median at 0.78 and ~80% of bursts have fractional flux values $\gtrsim$0.5, indicating a strong preference toward high fractional flux, though not as strong as previous studies of smaller samples indicated.
6. The host-normalized offsets and fractional fluxes are correlated, such that bursts at small offset ($\lesssim$0.5) occur exclusively on regions of high fractional flux ($\gtrsim$0.6) and bursts at larger offset show no preference for unusually bright regions, indicating that the preference for high fractional flux present in the full sample is entirely due to LGRBs at small offset.
7. The offset and fractional flux distributions show no statistically significant trends with redshift.

From our study it appears that the star formation occurring within $\sim R_h$ is the most favorable for LGRB production. The distribution of fractional flux for our sample of LGRBs agrees remarkably well with that for Type Ic SNe, a scenario that is consistent with the well-known connection between LGRBs and Type Ic-BL SNe. Both types of transients occur in special types of galaxies and in special environments within their hosts, where metallicity is likely not the only important factor. In the central regions of galaxies it is possible that changes in the IMF or increased massive star binary fractions may be responsible for the sub-galactic preferences of LGRBs and Ic-BL SNe. This new view of LGRB locations is unlikely to change in the near future because the sample size is unlikely to increase significantly. Progress toward understanding the precise factors at play in the central regions of LGRB host galaxies will likely come through studies of LGRB progenitor analogs in the local universe whose environments can be studied in great detail.

The Berger GRB group at Harvard is supported in part by the NSF under grant AST-1411763 and by NASA under grant NNX15AE50G. This paper is based upon work supported by the National Science Foundation Graduate Research Fellowship Program under Grant No. DGE1144152. W.F. acknowledges support provided by NASA through Einstein Postdoctoral Fellowship grant number PF4-150121 issued by the *Chandra* X-ray Observatory Center, which is operated by the Smithsonian Astrophysical Observatory for NASA under contract NAS8-03060. We thank Ragnhild Lunnan, Maria Drout, Josh Grindlay, and Avi Loeb for helpful discussions. The *HST* data presented here and the *Swift*/UVOT data used in this work were obtained from the Mikulski Archive for Space Telescopes (MAST). STScI is operated by the Association of Universities for Research in Astronomy, Inc., under NASA contract NAS5-26555. Support for MAST for non-*HST* data is provided by the NASA Office of Space Science via grant NNX09AF08G and by other grants and contracts. Based in part on observations obtained at the Gemini Observatory, acquired through the Gemini Science Archive, and processed using the Gemini IRAF package, which is operated by the Association of Universities for Research in Astronomy, Inc., under a cooperative agreement with the NSF on behalf of the Gemini partnership: the National Science Foundation (United States), the National Research Council (Canada), CONICYT (Chile), the Australian Research Council (Australia), Ministério da Ciência, Tecnologia e Inovação (Brazil) and Ministerio de Ciencia, Tecnología e Innovación Productiva (Argentina). Based in part on data obtained from the ESO Science Archive Facility. This paper makes use of data gathered with the 6.5 m *Magellan* Telescopes located at Las Campanas Observatory, Chile. This research has made use of data obtained from the

Chandra Data Archive and software provided by the *Chandra* X-ray Center (CXC) in the application package CIAO. Based in part on data collected at the Subaru Telescope and obtained from SMOKA, which is operated by the Astronomy Data Center, National Astronomical Observatory of Japan. We thank S.B. Cenko for providing Palomar 60 inch afterglow images for GRBs 060206 and 090618, T. Krühler and J. Greiner for providing GROND afterglow images for GRBs 080520, 081121, and 081109 and a WHT image for GRB 090113, D. Malesani for providing a TNG afterglow image for GRB 060605, D. A. Kann for providing a WHT afterglow image for GRB 060124, and D. Perley for providing a Keck telescope afterglow image of GRB 071010A and a Palomar 60 inch afterglow image of GRB 080607.

REFERENCES

Alard, C. 2000, A&AS, 144, 363
Beckwith, S. V. W., Stiavelli, M., Koekemoer, A. M., et al. 2006, AJ, 132, 1729
Berger, E. 2010, ApJ, 722, 1946
Bertin, E., & Arnouts, S. 1996, A&AS, 117, 393
Bloom, J. S., Kulkarni, S. R., & Djorgovski, S. G. 2002, AJ, 123, 1111
Bouwens, R. J., Illingworth, G. D., Oesch, P. A., et al. 2015, ApJ, 803, 34
Bromm, V., & Loeb, A. 2006, ApJ, 642, 382
Christensen, L., Hjorth, J., & Gorosabel, J. 2004, A&A, 425, 913
Christensen, L., Vreeswijk, P. M., Sollerman, J., et al. 2008, A&A, 490, 45
Cucchiara, A., Fumagalli, M., Rafelski, M., et al. 2015, ApJ, 804, 51
Faber, S. M., Willmer, C. N. A., Wolf, C., et al. 2007, ApJ, 665, 265
Frail, D. A., Kulkarni, S. R., Sari, R., et al. 2001, ApJL, 562, L55
Fruchter, A. S., Levan, A. J., Strolger, L., et al. 2006, Natur, 441, 463
Fryer, C. L., Woosley, S. E., & Hartmann, D. H. 1999, ApJ, 526, 152
Gonzaga, S., Hack, W., Fruchler, A., et al. 2012, The DrizzlePac Handbook (Baltimore, MD: STSci)
Graham, J. F., & Fruchter, A. S. 2013, ApJ, 774, 119
Hogg, D. W., Pahre, M. A., McCarthy, J. K., et al. 1997, MNRAS, 288, 404
Kelly, P. L., Filippenko, A. V., Modjaz, M., & Kocevski, D. 2014, ApJ, 789, 23
Kelly, P. L., & Kirshner, R. P. 2012, ApJ, 759, 107
Kelly, P. L., Kirshner, R. P., & Pahre, M. 2008, ApJ, 687, 1201
Krühler, T., Greiner, J., Schady, P., et al. 2011, A&A, 534, A108
Krühler, T., Malesani, D., Fynbo, J. P. U., et al. 2015, A&A, 581, A125
Le Floc'h, E., Duc, P.-A., Mirabel, I. F., et al. 2003, A&A, 400, 499
Levesque, E. M. 2012, in Proc. IAU Symp. 279, Death of Massive Stars, Supernovae and Gamma-Ray Bursts, ed. P. Roming, N. Kawai, & E. Pian (Cambridge: Cambridge Univ. Press), 167
Levesque, E. M., Berger, E., Soderberg, A. M., & Chornock, R. 2011, ApJ, 739, 23
Levesque, E. M., Kewley, L. J., Berger, E., & Zahid, H. J. 2010a, AJ, 140, 1557
Levesque, E. M., Kewley, L. J., Graham, J. F., & Fruchter, A. S. 2010b, ApJL, 712, L26
Lunnan, R., Chornock, R., Berger, E., et al. 2014, ApJ, 787, 138
Lunnan, R., Chornock, R., Berger, E., et al. 2015, ApJ, 804, 90
MacFadyen, A. I., & Woosley, S. E. 1999, ApJ, 524, 262
Marchesini, D., van Dokkum, P., Quadri, R., et al. 2007, ApJ, 656, 42
Mason, B. D., Hartkopf, W. I., Gies, D. R., Henry, T. J., & Helsel, J. W. 2009, AJ, 137, 3358
Metcalfe, N., Shanks, T., Weilbacher, P. M., et al. 2006, MNRAS, 370, 1257
Modjaz, M., Kewley, L., Bloom, J. S., et al. 2011, ApJL, 731, L4
Modjaz, M., Kewley, L., Kirshner, R. P., et al. 2008, AJ, 135, 1136
Ofek, E. O., Cenko, S. B., Gal-Yam, A., et al. 2007, ApJ, 662, 1129
Oke, J. B., & Gunn, J. E. 1983, ApJ, 266, 713
Perley, D. A., Levan, A. J., Tanvir, N. R., et al. 2013, ApJ, 778, 128
Perley, D. A., Perley, R. A., Hjorth, J., et al. 2015a, ApJ, 801, 102
Perley, D. A., Tanvir, N. R., Hjorth, J., et al. 2015b, arXiv:1504.02479
Planck Collaboration, Ade, P. A. R., Aghanim, N., et al. 2014, A&A, 571, A16
Podsiadlowski, P., Mazzali, P. A., Nomoto, K., Lazzati, D., & Cappellaro, E. 2004, ApJL, 607, L17
Pollack, L. K., Chen, H.-W., Prochaska, J. X., & Bloom, J. S. 2009, ApJ, 701, 1605
Prieto, J. L., Stanek, K. Z., & Beacom, J. F. 2008, ApJ, 673, 999
Ramirez-Ruiz, E., Lazzati, D., & Blain, A. W. 2002, ApJL, 565, L9
Sana, H., de Mink, S. E., de Koter, A., et al. 2012, Sci, 337, 444
Savaglio, S., Glazebrook, K., & Le Borgne, D. 2009, ApJ, 691, 182
Schlafly, E. F., & Finkbeiner, D. P. 2011, ApJ, 737, 103
Stanek, K. Z., Gnedin, O. Y., Beacom, J. F., et al. 2006, AcA, 56, 333
Svensson, K. M., Levan, A. J., Tanvir, N. R., Fruchter, A. S., & Strolger, L.-G. 2010, MNRAS, 405, 57
Thöne, C. C., Christensen, L., Prochaska, J. X., et al. 2014, MNRAS, 441, 2034
van den Heuvel, E. P. J., & Yoon, S.-C. 2007, Ap&SS, 311, 177
Vila-Costas, M. B., & Edmunds, M. G. 1992, MNRAS, 259, 121
Vreeswijk, P., Malesani, D., Fynbo, J., et al. 2008, GCN, 8301, 1
Wainwright, C., Berger, E., & Penprase, B. E. 2007, ApJ, 657, 367
Woosley, S. E. 1993, ApJ, 405, 273
Woosley, S. E., & Bloom, J. S. 2006, ARA&A, 44, 507
Zaritsky, D., Kennicutt, R. C., Jr., & Huchra, J. P. 1994, ApJ, 420, 87